BNL-219869-2020-INRE

24.1.3.1.1 - Frisch Grid CZT Spectrometer

A. Bolotnikov

September 2020

Nonproliferation and National Security Department

Brookhaven National Laboratory

U.S. Department of Energy

USDOE National Nuclear Security Administration (NNSA), Office of Nonproliferation and Verification Research and Development (NA-22)

DISCLAIMER

Safeguards Technology Development Program
Final Report
March 17th, 2020

WBS # – Project Title: 24.1.3.1.1 – Frisch Grid CZT Spectrometer

Lab – POC: BNL – Susan Pepper, Pepper@bnl.gov

Principal Investigator: BNL-- Aleksey Bolotnikov, bolotnik@bnl.gov , LLNL -- decman1@llnl.gov, LANL--Bill Geist, wgeist@lanl.gov, SRNL -- Ron Jeffcoat, ron.jeffcoat@srnl.doe.gov

HQ POC: Arden Dougan

Abstract

Brookhaven National Laboratory (BNL) worked with FLIR System Inc., the manufacturer of the nanoRAIDER, to develop a handheld field deployable detector based on the novel position-sensitive virtual Frisch-grid (VFG) Cadmium-Zinc-Telluride (CdZnTe or CZT) detectors (with 1% FWHM at 662 keV or better energy resolution). The detector called nanoRAIDER-VFG would be an improvement to the current nanoRAIDER, which is a compact gamma-ray detection instrument manufactured by FLIR Systems Inc. that employs relatively lower-performing CZT hemispheric detectors (i.e., 3%-FWHM CZT detectors). The nanoRAIDER-VFG would have significantly improved accuracy of measurements while maintaining similar efficiency, as compared to the nanoRAIDER, for in-field analysis of nuclear materials and detection of undeclared activities during inspections conducted by the International Atomic Energy Agency (IAEA). Since the nanoRAIDER is currently used by the IAEA as part of its Complementary Access toolkit, a relatively quick acceptance of the nanoRAIDER-VFG for safeguards was anticipated. The nanoRAIDER-VFG project was undertaken to address the following items in the IAEA's Long-Term R&D Plan, 2012-2023: 2.2 (elemental and isotopic signatures of fuel cycle processes); 2.3 (detect signatures of undeclared activity and improve analysis); and 2.6 (detect process emanations). The high energy-resolution of the nanoRAIDER-VFG would also have had applicability to 3.2 (fissile content of metal mixtures containing actinides Np, Am, etc.). The project was not completed due to a change in priorities within FLIR.

1. BACKGROUND

The nanoRAIDER-VFG was proposed for use by safeguards inspectors on inspections. It offers an improved capability for detection, localization, and identification of the gamma and neutron radiation signatures of undeclared nuclear and other radioactive materials and related activities, as well as for the verification of the presence and identity of nuclear materials declared pursuant to Article 2 of INFCIRC/540. It was planned that it would also provide reasonably accurate measurements of the gamma dose rate and the neutron count rate for personal radiation hazard awareness.

The nanoRAIDER-VFG incorporates a CdZnTe (CZT) Virtual Frisch-grid (VFG) detector array (with <1% or better resolution) into an existing platform (called nanoRAIDER-AVG) to achieve improved performance in safeguards applications. The new device was to be made commercially available by FLIR. The bench-top demonstration system developed in FY17-19 was based on 2x2, 4x4, and linear arrays of 6x6x20, 4x7x25, and 8x8x32, and 10x10x32 mm^3 position-sensitive VFG detectors. Such a variety of arrays and detector dimensions helped us to evaluate the novel detector technology and identify optimal detector configurations for future instruments.

The main advantage of the position-sensitive VFG detectors is that they can employ standard- (not specially selected) grade CZT material and still achieve high-energy resolution (1% or less FWHM at 662 keV), large effective area, and low-power consumption. This development was motivated by the high cost and low availability of large, > 1 cm^3, CZT crystals suitable for making multi-pixel detectors with acceptable energy resolution and efficiency.

Figure 1 shows a photo of the nanoRAIDER (a) and a sketch of the proposed nanoRAIDER-VFG (b). The proposed instrument functional elements and expected performance characteristics are summarized in Table 1.

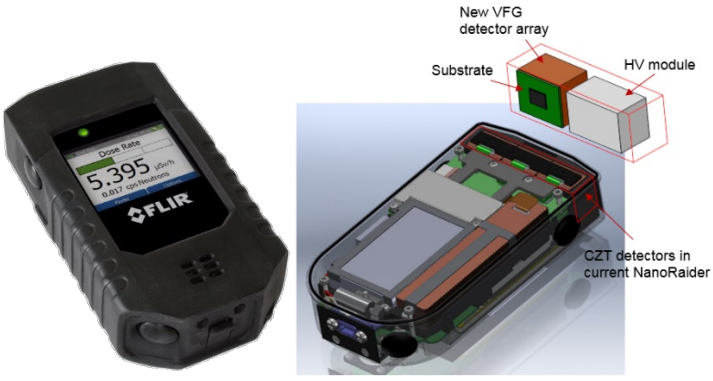

(a) (b)

Figure 1. (a) Photo of the nanoRAIDER; and (b) Sketch of the proposed nanoRAIDER-VFG.

Table 1: Instrument Functional Elements

Weight: <1 lb
Portability: wearable and handheld
Operating environment: indoor and outdoor; -25 °C to 50 °C
Data logging: internal memory for 600,000 spectra
Communication: USB 2.0 (mini-B socket) and Bluetooth
Energy Range (Gamma): 30 keV to 3 MeV
Energy Range (Neutron): thermal
Energy Resolution: <1% FWHM at 662 keV and <2% at 186 keV
Efficiency: About 2x compared to the current nanoRAIDER
Data analysis and reporting: embedded software for data analysis, spectrum visualization and isotope identification
Power requirements: 100-240 VAC (USB cable with wall and car adapters); 1800 mAh Li-ion battery
Typical measurement time: Depends on source activity, shielding and standoff distance; typically, 5-60 minutes.

The nanoRAIDER-VFG device will work as a wearable or handheld device in the field. It can operate as a stand-alone device with self-contained software for spectral analysis and isotope identification and the LCD screen for data visualization and information display. In addition, it can communicate with a computer via USB or Bluetooth, so data can be downloaded to computer and further maintained in a user database. Given the high energy resolution of VFG detectors, the nanoRAIDER-VFG will be the highest performing Spectroscopic Personal Radiation Detector (SPRD). To reduce the training burden on first responders and security personnel, the nanoRAIDER-VFG will use the same firmware as in the nanoRAIDER for its user interface. With a few button controls, operators can pick up the device and begin using it simply and quickly.

2. BRIEF PROJECT DESCRIPTION AND PARTICIPANTS CONTRIBUTIONS

We proposed to use the existing capability and infrastructure at BNL and FLIR to integrate and test the new nanoRAIDER-VFG handheld instrument that would be an improvement to the current nanoRAIDER developed by FLIR. The first BNL's task of the project was to design and build a 2x2 array of 6x6x20 mm^3 CZT detectors and the readout system based on the existing AVG1 ASIC developed by BNL for virtual Frisch-grid detectors. Following to our original schedule BNL designed a new detector board, a detector holder to support 2x2 detector array, and a data interface between the BNL's readout electronics and HM-5 instrument. All three components were fabricated and delivered to FLIR for the further tastings. BNL and FLIR jointly developed design specifications of the nanoRAIDER-VFG. FLIR conducted engineering design, fabricated and tested several key components and the first benchtop prototype during FY2016.

Several tests were carried out at BNL and LLNL using the developed arrays and the BNL's benchtop readout system, which demonstrated the feasibility of the future instrument. These detectors tests at BNL and LLNL along with the hardware components evaluations at FLIR helped us to finalize the instrument design and came up the plan for FY2017 and FY2018. The formfactor and the instrument was redesigned and aligned to the commercial FLIR's R200 instrument. The new name for the proposed instrument was selected, R200-VFG. We examined the test results of the current nanoRAIDER-VFG bench-top system and developed the design specifications of R200-VFG hand-held device. FLIR upgraded the power supply circuits/battery in the R200 device accordingly to match the new power specification. A new high-voltage (HV) module will be added as well to bias the CdZnTe detectors. We examined the overall heat generated by the new device, including the readout electronics for the detectors, the new power supply circuits and other components related to data acquisition/collection and communication. We redesigned the packaging of the detectors and other components – readout electronics, battery, HV module and device control circuits. In addition, BNL conducted qualification tests with the device, finalizing all the designs, and generating all the design documentation for transitioning CZT detector technology to industrial partners via a CRADA or other arrangements.

The instrument was expected to be ready for evaluation measurements at Savannah River National Lab and the Westinghouse Fuel Fabrication Facility (WFFF) during FY2017. However, this task was not completed as planned. The test was first postponed till the end of FY2018 and then moved further beyond the duration of the project. The initial schedule was adjusted due to delays at FLIR. Even though FLIR was very interested in the successful completion of the project, their progress was often interrupted and delayed due to FLIR's internal projects and production. To keep the project moving ahead, BNL integrated two detectors employing 2x2 and 1x6 arrays (mounted inside a temporary enclosure) were successfully used for UF6 cylinder measurements at WFFF alongside the conventional HM-5 instrument. Even though the FLIR prototype was not ready for these tests, the BNL prototypes demonstrated the high performance of the VFG detector arrays for enrichment measurements of UF6 cylinders in field environments and their potential for use in practical handheld instruments.

The list of completed tasks and the project participants contributions are summarized below.

FY2015:

We started the project in FY15 by analyzing IAEA needs, understanding future detector requirements and evaluating performance of position-sensitive VFG detectors, including:

1. Familiarization with the HM-5 and nanoRAIDER device architectures;
2. Integration and testing of several 2x2 and 3x3 detector arrays;
3. Demonstrate data with BNL's VFG detectors and data-acquisition system and FLIR's software for energy spectra and isotope ID;
4. Conduct tests on bench-top units and data acquisition systems.

FY2016:

After demonstrating the high energy-resolution spectroscopic capability of VFG detectors in FY15, this project focuses on the following tasks:

1. Fabricate VFG detector arrays for the new nanoRAIDER VFG devices;
2. Develop an interface between VFG detector array plus its readout electronics and the data acquisition platform at FLIR;
3. Assemble and test new devices in laboratory environment and in the field;
4. Two detector modules have been fabricated for FLIR;
5. The adaptor printed circuit board was developed and delivered to FLIR;
6. FLIR built and tested an engineering prototype;
7. An engineering prototype was built and tested in BNL

FY2017:

During FY17 BNL developed and tested several types of position-sensitive VFG detector arrays suitable for compact hand-held instruments. LLNL continued software development and analyzing data. The major tasks included:

1. Integrated and tested a linear 1x6 array and two square 2x2 and 4x4 arrays;
2. A CRADA agreement has been signed with FLIR, which laid out a pathway for our collaboration that will transfer our novel technology to commercial development;
3. Continued helping FLIR to integrate the first prototype of the hand-held prototype;
4. Finalized the interface between the VFG detector array and the FLIR data acquisition platform and delivered it to FLIR;
5. Transferred the BNL firmware and software to FLIR, assembled two test boxes and delivered them to FLIR, and assisted FLIR in testing and development of signal processing software;
6. Carry out two field measurements at LLNL, SRNL and the Westinghouse Fuel Fabrication Facility at Columbia, SC. The main goal of these measurements was to demonstrate the feasibility of enrichment measurements of the UF6 storage cylinders (LANL, LLNL, SRNL, and BNL were involved in these measurements);
7. LLNL analyzed the data for the UF6 cylinders measured at the Westinghouse Fuel Fabrication Facility (WFFF), including the initial analysis of the data acquired by the HM-5.

FY2018:

During FY18 BNL fabricated and tested additional detectors for FLIR, while FLIR continued integrating the instrument prototype to meet the task milestones:

1. The FLIR team made progress with the hardware design for processing signals of a CZT detector with 6 electrodes;
2. Raw detector signals were acquired with this setup;

3. The crystal with dimensions of 5x5x15mm studied was cut from an R300 15x13x5mm CZT detector;
4. BNL investigated performance of the new 4x4 array modules, developed for the high energy gamma ray Compton camera, for spectroscopy of the low-energy gamma rays used in enrichment measurements;
5. LLNL continued to analyze the data for the UF6 cylinders measured at the Westinghouse Fuel Fabrication Facility;
6. LLNL and BNL worked together to better understand the discrepancy in the data obtained for the UREU1004477 cylinder;
7. The problem with the data discrepancy, attributed to the readout system firmware, was resolved by upgrading the user interface and implementing the new firmware.

FLIR completed most of the project's tasks, including the instrument design, benchtop testing of the components, selecting electronics, and testing detector arrays using BNL waveform digitizing system. Most of the project milestones have been met. BNL and FLIR completed the detector array design and optimization, the instrument's mechanical design, readout electronics and the signal processing algorithm. LLNL and LANL worked on software development and enrichment calculation software tasks. The hardware and software components were delivered to FLIR according to the schedule. The data from the detector testing were analyzed and provided to NA-241.

However, the final integration of the instrument prototype has not been completed. Even though the project did not produce a fully functional prototype, the team completed most of the tasks required for the final instrument integration. The instrument testing, expected to take place in September of 2018, was postponed due to delays in the prototype assembly at FLIR. Even though FLIR continued to express interest in the project and the new instrument, it became apparent that it was difficult for FLIR to direct adequate resources to the project. The dependence on the internal company management decisions made the entire project vulnerable and prevented BNL from keeping the project on schedule and completing it within the allocated budget. We expect that FLIR will continue this development in the future using its own resources. The ultimate goal of testing the FLIR prototype at the Westinghouse Fuel Fabrication Facility (WFFF) was postponed and moved further beyond the duration of the project. The NA-241 program manager interpreted the lack of communication as a lack of interest and decided to close the project.

Nevertheless, the project team made a significant progress in further development of position-sensitive VFG detectors and associated technology that have great potentials for the future gamma-ray detectors. Next we present a detailed summary of the developed technology.

2.1 POSITION-SENSITIVE VIRTUAL FRISCH-GRID DETECTORS

Arrays of position-sensitive virtual Frisch-grid (VFG) CdZnTe (CZT) detectors offer an economical way to produce large area, high detection efficiency and high energy resolution gamma cameras. The correction of response non-uniformity caused by crystal defects allows the use of standard-grade (unselected) CZT crystals, which results in a dramatic reduction in the instrument's cost. The arrays provide performance and functionality comparable to 3D pixelated detectors but at a lesser cost. The potential applications of the arrays, which can be configured into detection planes with different geometrical form factors and dimensions, includes nonproliferation, safeguards, gamma-astronomy and

other areas which require spectroscopy and imaging of gamma-ray sources in a wide dynamic range, from ~10 keV up to several MeV.

The majority of CZT spectroscopic detectors employ VFG designs to achieve their spectroscopic preferences. There are a number of designs described in literature: 3-terminal [1], CAPture [2], hemispherical [3,4], capacitive Frisch-grid [5,6], pixelated [7,8], and their modifications. The main distinguishing feature of our detectors is their geometry; we use bar shaped CZT crystals with a large aspect ratio and relatively small, ~6x6 mm^2, cross-section. Arrays of such bars can substitute for large CZT crystals, which are expensive and difficult to produce. In contrast, the bars can be fabricated using the standard 6-mm thin CZT wafers, which are mass-produced by both eV-Products and Redlen Technologies for medical imaging and baggage screening instruments.

We started our development by using conventional VFG detectors (without position-sensitive pads) made of 15-mm long bars [9]. For these arrays, we typically achieved < 1.5% FWHM at 662 keV in the laboratory and after the drift-time corrections. Moreover, when we used carefully selected, high-homogeneity crystals, we obtained < 1% resolution. However, this performance improvement came at the higher detector cost. To increase the acceptance rate of CZT crystals and reduce instrument costs we proposed the position-sensitive VFG detectors, which allowed us to correct response non-uniformity by virtually dividing the detector volumes into small voxels and equalizing the responses from each voxel. We described the design and fabrication procedure of position-sensitive VFG detectors and arrays of such detectors in our previous publications [10-13]

2.2 VFG DETECTOR DESIGN

Our position-sensitive VFG detectors are based on the use of capacitive (or non-contacting) Frisch-grid. We modified the originally proposed capacitive Frisch-grid [5,6] detectors by employing high-aspect ratio CZT crystals, reducing the width of the capacitive-shielding electrode to 5 mm, and placing it right at the anode side edge (Fig. 1). The electrode's width was optimized to provide a good electrostatic shielding of the anode (for the crystals with an aspect ratio greater than 3) while leaving the cathode unshielded, which means that the cathode signals become sensitive to the interaction depth and can be employed to correct the charge losses as the electrons' cloud drift from the origin point towards the anode. We grouped detectors into 4x4 arrays with the common cathode to increase the cathode sensitivity. Next, we divided the shielding electrode at the anode into 4 segments (pads), each on one side of the crystal. In practice, we encapsulate the crystal bars into ultrathin, 100-200 µm, polyester shells and glue the metal pads, cut from copper or aluminum tape. Two spring CuBe contacts are placed on the cathode anode sides and secured by means of the polyester shell enveloping the contacts around the edges. To protect the anode and cathode surfaces from any potential scratches during the encapsulation we placed a thin layer of conductive rubber or aluminum foil underneath the spring contacts (Fig. 3 below).

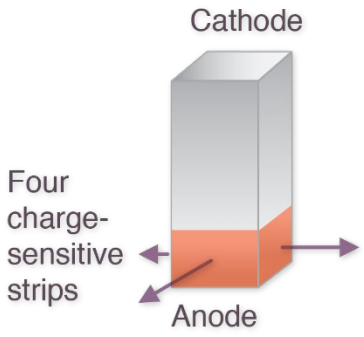

Fig. 3. Schematic of the position-sensitive VFG detector

Fig. 4 shows examples of the waveforms captured from the cathode, anode and pads signals (charge signals after charge-sensitive preamplifiers) for an event produced at some distance from the anode and close to one of the pads, X_2. The sum of the pad signals is also shown in the upper right corner. Each waveform has 1000 samples recorded with 8 ns/point [9,10]. The pad amplitudes should be calculated with respect to the negative pad levels. The negative steps of the pad signals correlate with *X-Y* coordinates, while the positive steps correlate with Z coordinates. The latter is reflected in the sum of the pad signals, whose front edge is almost identical to the cathode signal and can be used instead of the cathode signal. It this case, reading the cathode signals can be avoided. We note that it is very important for accurate position measurements that all pads samples were taken at the same time.

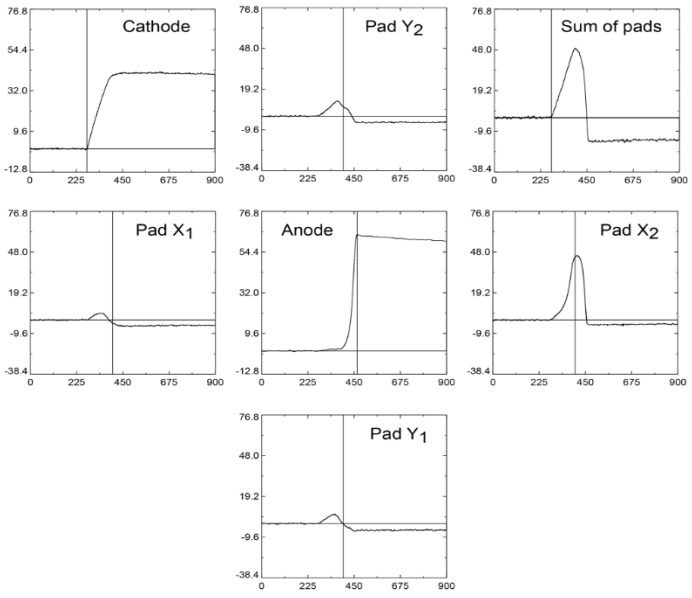

Fig. 4. Representative waveforms of the cathode, anode and pads signals generated for an event occurred at some distance from the anode and close to one of the pads, X_2. The sum of the pad signals is also shown in the upper right corner. Each waveform contains 1000 samples recorded every 8 ns.

The signal amplitudes and timing evaluated from the captured waveforms were used to generate the correlation plots illustrating the operational principles of position-sensitive VFG detectors. As an example, Fig. 5 shows such plots for the 10x10x32 mm^3 detector irradiated with an uncollimated Cs^{137} source. The detector under test was biased at 3500 V. The dependences of the anode signals versus the cathode-to-anode ratio, *C/A*, (a) and the sum of the pads to anode, *P/A*, (b) ratios look very similar, demonstrating that the sum of the pad signals can substitute for the cathode signals. Both dependences can be used to apply the interaction depth (1D) corrections. The dependence of the anode amplitudes versus the drift time (c) can also be used to correct the charge loss along the Z direction. The first line in the anode vs. drift time distribution (c) indicates approximately the position of the virtual Frisch-grid. The second line indicates the edge from the events interacting near the cathode corresponding to the maximum drift time, when carriers drift from the cathode to the anode. The anode amplitudes from the 662-keV photo absorption events taken at the maximum drift time correspond to the total collected charge (after drifting the entire length of the crystal) unaffected by the holes (for the events near the cathode the holes are completely shielded). Finally, the correlation between the cathode-to-anode ratio and the drift time (d) illustrate that the *C/A* (or *P/A*) ratios and the drift time give two independent estimates for the *Z* coordinates. To complete the picture, we also show frequency distributions of *C/A* ratio (e) and drift times (f).

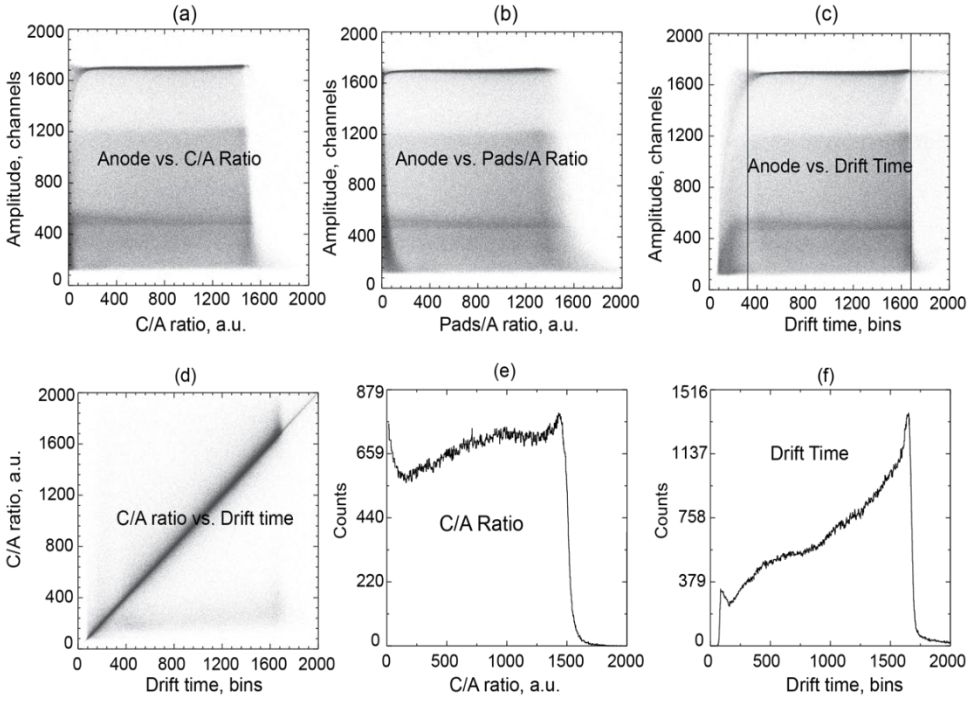

Fig. 5. The dependences of the anode amplitudes versus the drift time (c) can also be used to correct the charge loss along the *Z* direction. The first line in the anode vs. drift time distribution (c) indicates the approximate position of the virtual Frisch-grid. The second line indicates the edge from the events

interacting near the cathode corresponding to the maximum drift time when carriers drift between the cathode and the anode.

2.3 READOUT ELECTRONICS

We developed the second generation of the AVG ASIC [9] optimized for position-sensitive VFG detectors. The original AVG1 ASIC was developed to work with conventional VFG detectors. It had 36 anodes and 9 cathode inputs, and its architectural design was adopted from its predecessor, the H3D ASIC, developed for 3D pixelated detectors by BNL's Instrumentation Division in collaboration with the University of Michigan [16-17]. The new generation ASIC (AVG2) has 48 identical anode/pad channels and 4 cathode channels. The main difference from the AVG1 is that its inputs can be configured for reading either the anodes (positive signals) or pads (negative signals). As its predecessor, AVG2 implements the conventional processing chain of analog signals including a low-noise charge-sensitive amplifier with continuous reset, a baseline stabilizer, a fifth-order unipolar shaping amplifier with an adjustable peaking time, and two peak and timing detectors for measuring the amplitude and timing for both the positive and negative pulses. Several gain settings (20, 40, 60, and 120 fC/mV) are available with the maximum dynamic range up to 3 MeV at the lowest gain. The cathode channel also has a charge-sensitive amplifier with continuous reset and a baseline stabilizer. It is followed by two parallel filtering circuitries: one (with a long shaping time) for measuring the amplitude, and the other (with a short shaping time) for measuring the timing. The timing assigned to the anode signals is measured at their peaking time and is, to a first order, independent of the signal amplitude.

The ASIC is mounted on the fanout board with the contacting pads on its back side matching the contacting pads on the detector board, see Fig. 4. As previously mentioned, the ASIC and detector boards with the Samtec Z-Ray [14] interposer in between are bolted together to the aluminum frame. The back side of the ASIC board has two multi-pin connectors that allow the assembled array to be plugged into the readout system's motherboard mounted inside the test box. This readout system was originally designed for H3D [8] detectors and was also used for our first array prototypes [9]. For the negative signals captured from the pads, we used a short peaking time of 0.25 μs matching to the short drift time of the electron cloud between the virtual Frisch-grid and the anode. The short shaping time also minimizes the contribution of the slow-rising positive front of the pad charge signal being induced by the electrons before they reach the virtual Frisch-grid, which strongly depends on the interaction depth. For the anode and the cathode signals, we used 1-2 μs peaking time which is a good compromise between the electronic noise and the ballistic deficit effect. It is worth mentioning that the electron drift time across a 20-mm thick CZT detector is 1.5-1.7 μs at the typical cathode bias of 2.5-3 kV. Any detector from the array could initiate the readout sequence from all channels. For each interaction event, the ASIC provides the peaks' amplitudes (positive and negative) and the corresponding times captured in all detectors. The data is saved in the computer's memory and processed off-line.

2.4 DETECTORS CALIBRATION

To calibrate detectors, we irradiated arrays with uncollimated gamma-ray sources with well-defined gamma-lines to cover the low- and high-energy ranges, i.e., 238 and 662 keV photopeaks generated by ^{232}U and ^{137}Cs. First, we evaluated the input baselines by fitting the noise peaks on the leftmost side of the

pulse-height spectra. Then using the cathode-to-anode and the pad-to-anode ratios we virtually segmented each detector into many voxels, typically between 20x20x20 and 60x60x60, dependent on the crystal quality. Finally, we plotted the pulse-height spectra generated from each voxel and equalized their gains by aligning the photopeaks at the same positions. The corresponding gain-scaling coefficients were stored into 3D matrixes (look up tables) used to apply corrections to the raw data on-the-fly to equalize the detector responses. We called this the 3D correction versus the 1D correction, representing the conventional drift time or interaction-depth corrections. The temperature dependence of the detector responses was taken into account by generating several correction matrixes at different temperatures. We note, however, that the correction matrix is a product of two matrixes. One takes into account the response variations relative to the anode signal and is independent from the photon energy and temperature. The second takes into account the gain variations of the detectors and their dependence on the temperature. The temperature dependence of the detector gains should be measured during the calibration and adjusted accordingly using a linear interpolation. Alternatively, one can stabilize the detector operating temperature point.

2.5 SPECTROSCOPIC PERFORMANCE

The main advantage of position-sensitive CZT detectors is the ability to use the position information to correct the detectors' response non-uniformities and improve their spectral performances. Using position information, we can virtually divide the VFG detector into small voxels, so small that we can assume uniform responses within individual voxels. Therefore, in order to correct the response of the entire detector, one just needs to adjust the "gains" of the individual voxels. The corresponding scaling coefficients, which must be generated during the detector calibration, are stored in a 3D look-up matrix and used to correct, in-fly, the measured amplitudes in accordance with the measured X-Y-Z coordinates. We called this the 3D correction versus the 1D correction representing the conventional drift time or interaction-depth corrections. The calibration is done in a reverse order. Using a large set of data obtained, for instance, with the ^{137}Cs test source, we generated pulse-height spectra from the individual voxels and equalized their responses by aligning the photopeaks at the same channel number [4]. We note that it is important to use different data sets for calibration and for plotting the results. Otherwise, the correlation between the correction matrix and data will result in erroneously good spectra.

Figure 6: Illustration of 3D corrections

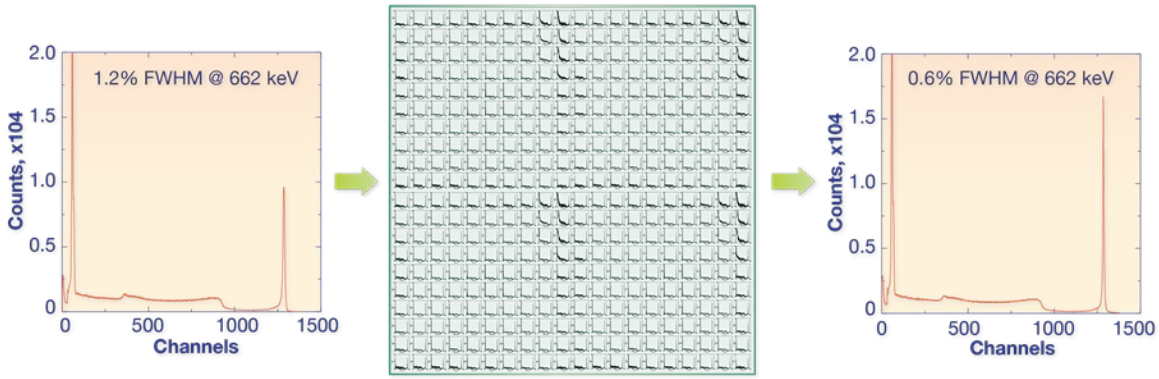

Several array configurations of VFG detectors have been tested: single detectors with dimensions up to 10x10x32 mm^3, 2x2, 4x4 and linear detector arrays of 6x6x20 and 5x7x25 mm^3 detectors (described next)

2.5.1 4x4 array of 6x6x20 mm^3 VFG detectors

As an example, Fig. 7 shows the design of the 4x4 array placed inside a G10 holder used for prototyping. This conceptual design, after some modifications required to reduce its dimensions and increase its robustness, was proposed for the final nanoRAIDER-VFG instrument. Each detector is slipped into a square cell formed by four vertical CuBe finger-spring contacts soldered directly to the fanout (detector) board. The finger-spring contacts connect the pads to the ASIC readout inputs. In this design, the gaps between the physical edges of the detector crystal can be potentially minimized to below 0.5-0.7 mm. To reduce the number of readout channels and simplify the array design, we connected the adjacent detectors facing each other's pads to the same contact. This may cause an ambiguity problem when interactions occur in two adjacent detectors. In such cases, we cannot use signals captured from the common pads, but the signals from the other two or three pads can be used to evaluate the positions of the interaction points. The signals just from two orthogonal pads are enough to measure the coordinates; this is further explained in section 4. The anode board is bolted to a 5-mm aluminum frame housing, and the detectors are attached on top with a 15-mm thick insulating frame made from G10 fiberglass. After inserting the detectors, the cathode board is used to gently press the detectors to the anode board. The spring contacts connect the anodes and the cathodes to the corresponding pads on the anode and cathode fanout boards. The cathode board, with four 50 pF decoupling capacitors and four 100 MΩ resistors (typically biased to 2.5-3 kV), is bolted to the top of the insulating frame with 8 plastic screws to ensure a uniform distribution of the load.

The back side of the ASIC board has two multi-pin connectors and can be plugged into the motherboard of the readout system. The motherboard carries the ultra-stable low-voltage passive converters supplying power to the ASIC chips, two analog-to-digital converters (ADCs) for digitizing the peak amplitudes and timing information from all channels, the Field Programmable Gate Array (FPGA) for processing the data and communicating with the ASICs, and the USB port.

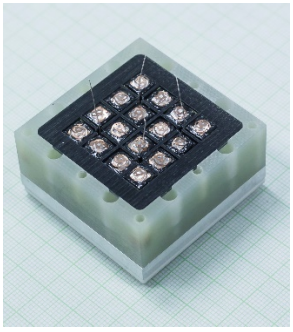

Fig. 7. Design of the array module used for prototyping.

For testing the arrays, we acquired 6x6x20 mm^3 standard-grade (unselected) CZT crystals from Redlen Technologies and eV-Products. The only requirement specified was the maximum leakage current, < 25 nA at 3,000 V and 25°C. The arrays were plugged into the motherboard of the readout system and enclosed inside an aluminum box. During the measurements, we placed the test box inside an environmental chamber to maintain the detectors at a specified constant temperature during the

measurements. We used uncollimated ^{137}Cs, and ^{232}U sources normally placed 2-3 cm above the array cathode board to generate signals inside the detectors. The cathode's bias was set at 2,500-3,000 V. The detectors' electronic noise, measured at high voltage on the cathode using the test-pulse signals, was found to be in the range of 2.5-3.5 keV, which is equivalent to 0.5-0.6% FWHM at 662 keV at 26°C.

Fig. 8 (a) shows the pulse-height spectra measured from ^{232}U and ^{137} Cs uncollimated sources with one of the 4x4 arrays. It shows spectra from 16-detectors biased at 2,800V and the temperature. The combined spectra after 1D and 3D corrections are shown in Fig. 8 (b and c), respectively. The energy resolutions evaluated for 286 and 662 keV lines of the 3D corrected spectrum were 1.8% FWHM at 200 keV and < 0.9% at 662 keV at 23°C. In the case of just 1D correction, we obtained 2.8% and 2.5% respectively. The raw (uncorrected) spectra (not shown) typically resulted in 3-6% energy resolution range at 662 keV. The main factor limiting the energy resolution of the VFG detectors, in comparison to H3D pixelated detectors, is electronic noise primarily related to the high leakage current, 5-25 nA, and large anode capacitance, ~3 pF on anodes. This is the trade-off for using less expensive CZT crystals in the detectors. The leakage current depends on the operating temperature. As we demonstrated previously [18-20], the detector's energy resolution stays below 1% FWHM at 662 keV for temperatures up to ~30 ^{0}C.

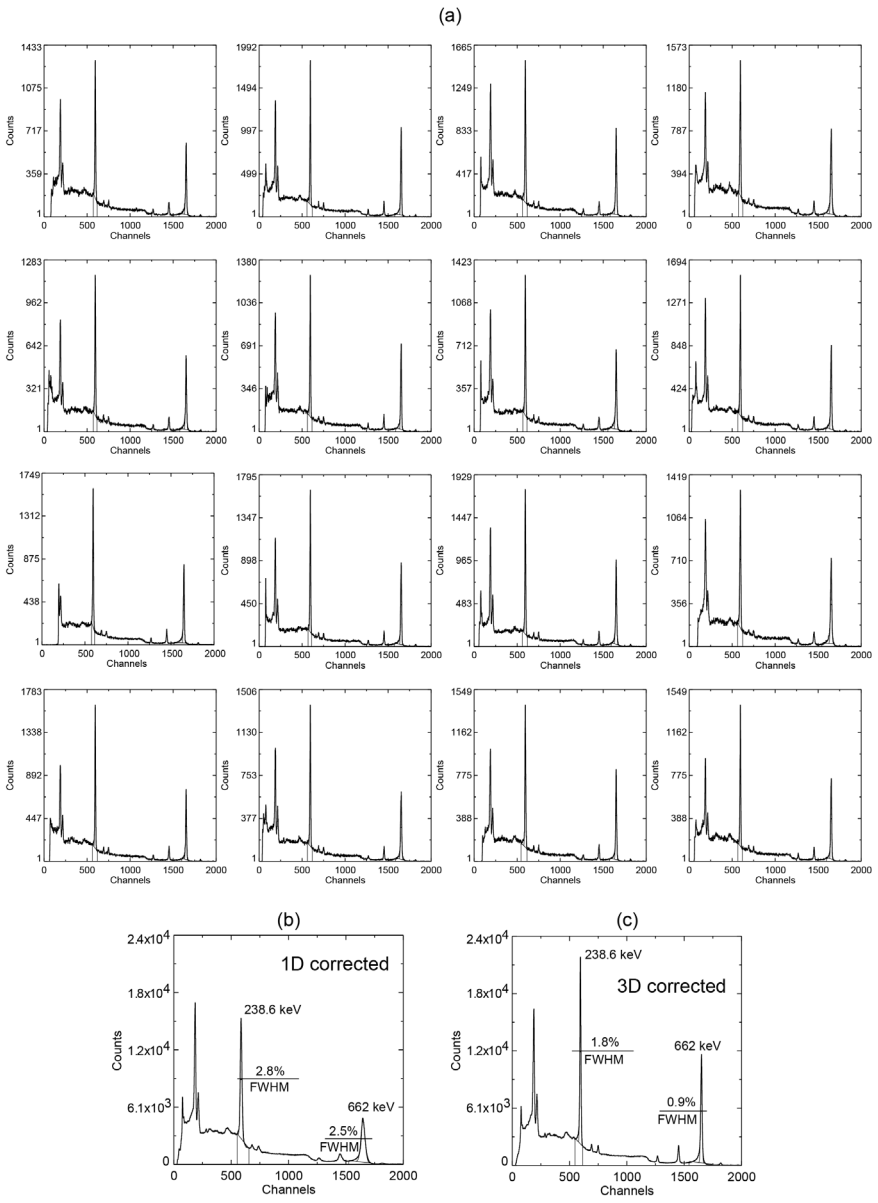

Fig. 8. Pulse-height spectra measured from ^{232}U and ^{137}Cs uncollimated sources with the 4x4 array module: (a) spectra measured from 16-detectors after 3D corrections, (b) the combined spectra after 1D and (c) after 3D corrections. The energy resolutions evaluated for 286 and 662 keV lines of the 3D corrected spectrum were 1.8% FWHM at 200 keV and < 0.9% at 662 keV at the detector temperature of 23 C. In the case of just 1D correction, we obtained 2.8% and 2.5% respectively. The raw (uncorrected) spectra (not shown) typically ranged between 3-6% at 662 keV.

Figs. 9 (a,b) shows the combined spectra (after 3D correction) measured from different sources: (a) the low-energy spectra measured at the gain of 120 fC/mV from the ^{57}Co source and (b) the gain of 60 fC/mV from the ^{232}U and ^{133}Ba sources. The cathode bias was 2800 V and the measurements were taken at 23 C. We obtained the energy resolution of 3% at 122 keV, 1.8% at 238.6 keV and 1.3% at 356.0 keV. The energy resolution degrades slightly at the lowest gain due to stronger contribution of the pickup noise generated by the readout system.

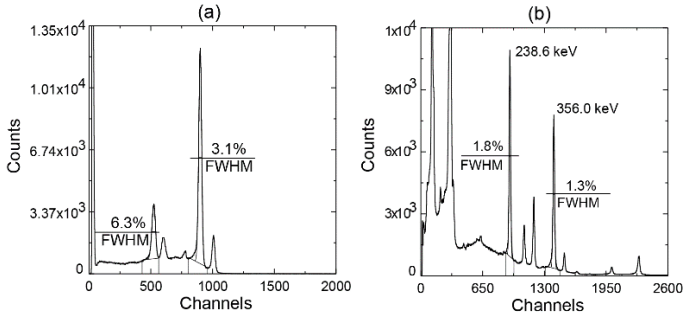

Fig. 9. Low-energy spectra measured at the gain of 120 fC/mV from the ^{57}Co source and the gain of 60 fC/mV from the two ^{232}U and ^{133}Ba sources at the detector temperature of 23 C. The cathode bias was 2800 V.

To evaluate the sensitivity of the array we carried out measurements using the standard 9.6 μCi ^{137}Cs source placed at several distances from the detector's cathode board, 1.0, 1.3, 1.6, and 2.0 m in the lab environment. The averaged minimum time to detect the 10 μCi source at 1 m was found to be (8 +/-1) s at 3 sigma (or 32 s at 6 sigma) confidence level. Fig. 10 shows the combined spectra measured from ~1 kg of U ore bag placed ~10 cm from the top surface of the array: (a) gain is 120 fC/mV, accumulation time is 7 h; (b) gain 60 fC/mV, accumulation time 25 min. The cathode bias is 2800 V and the detector's temperature is 23 C.

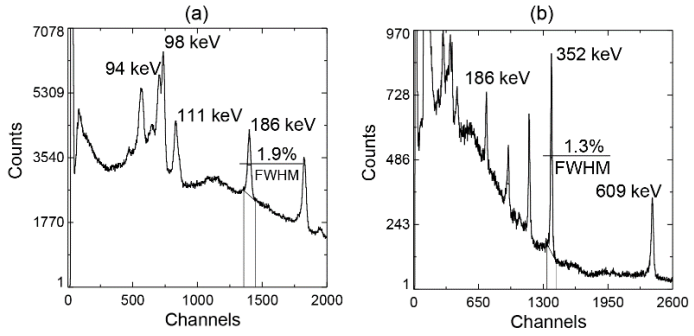

Fig. 10. Spectra measured from ~1 kg of U ore placed ~10 cm from the top surface of the array: (a) gain is 120 fC/mV, accumulation time is 7 h; (b) gain 60 fC/mV, accumulation time 25 min. The cathode bias is 2800 V and the detectors temperature is 23 C.

2.5.2 Large volume CZT detectors (8x8x32 and10x10x32 mm^3)

Large position-sensitive VFG detectors are very beneficial for use in hand-held instruments because they provide high detection efficiency with a minimum number of readout electronics. We have tested several 8x8x32 and 10x1032 mm^3 detectors that recently became available from Redlen Tech. Here we present some results from testing a ultra-thick CZT detectors, 10x10x32 mm^3. The measurements were

taken at the temperature of ~23 C and various cathode biases between 200-3500 V. The typical electronic noise, measured at ~3000 V bias on the cathode using the test-pulse signals, was found to be in the range of 4-5 keV FWHM (relatively high due to long wires used to connect the detector contacts), which is equivalent to 0.8% FWHM. Fig. 11 illustrates improvement of energy resolution after applying 1D and 3D corrections. The energy resolution improves from 3.6% (raw data) to 0.9% FWHM at 662 keV (after 3D corrections).

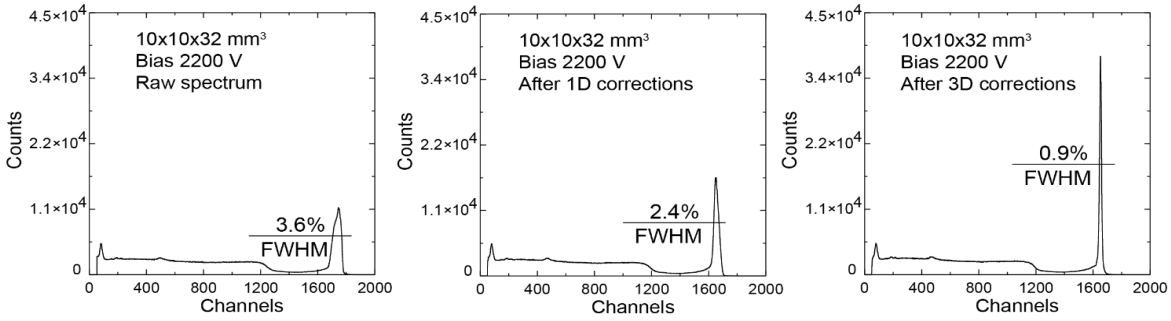

Fig. 11. The ^{137}Cs spectra after 1D and after 3D corrections for the 10x10x32 mm^3 detector biased at 2200 V.

Fig. 12 shows several representative spectra (after 3D corrections), acquired from ^{133}Ba, ^{60}Co and ^{232}U sources for 8x8x32 mm^3 and a 10x10x32 mm^3 detector. All detectors tested in this work showed very similar responses. The ^{232}U spectrum (in linear and logarithmic scales) was measured using a 5-mm lead shield to reduce low energy counts. The cathode bias was 3200 V for all the detectors. For the low-energy 356-keV line, we obtained 1.5% and 0.5% for the high-energy gamma at 2.6 MeV. We note that two 10x10x32 mm^3 detectors have the same volume as one 20x20x15 mm^3 H3D detector with comparable spectroscopic performance but require only nine readout channels.

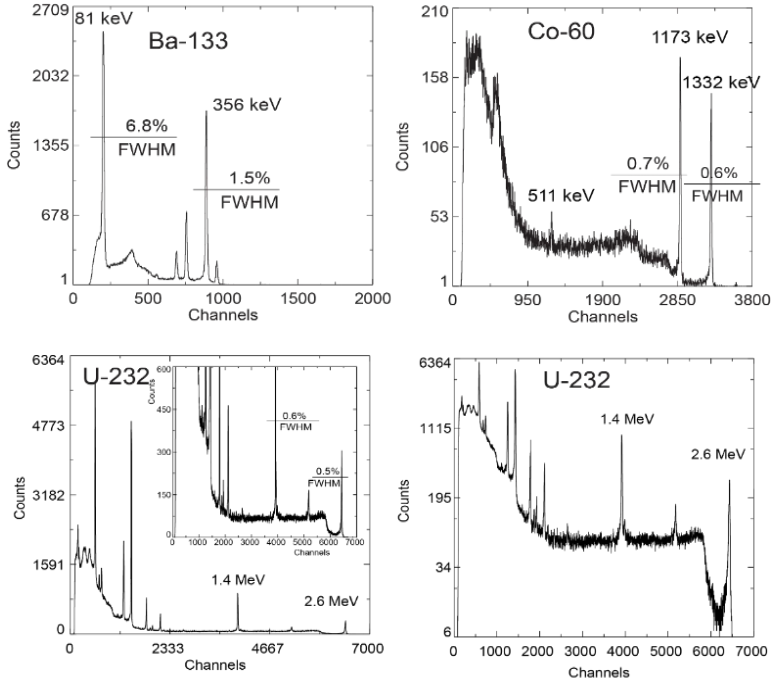

Fig. 12. The ^{133}Ba ^{60}Co and ^{232}U spectra measured from the 8x8x32 mm^3 (top) and 10x10x32 mm^3 (bottom) detectors biased at 3200 V at the temperature of ~23 C. The energy resolution (% FWHM) is 6.8% at 81 keV, 1.5% at 356 keV and 0.5% at 2.6 MeV.

Figure 13 presents ^{137}Cs pulse-height spectra measured from one of the 10x10x32 mm^3 detectors biased at 1600, 2200 and 3000 V. As seen, the detector performance remains practically unchanged down to 1600 V, illustrating good material uniformity and high electron mu-tau product. It also demonstrates that the detectors can operate at reduced biases, which is important for making practical instruments. We note, however, that for good imaging capabilities it is always better to operate CZT detectors at higher biases.

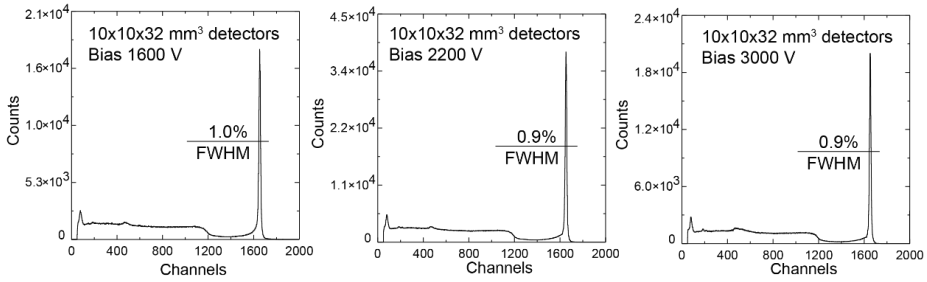

Fig. 13. ^{137}Cs pulse-height spectra measured from a 10x10x32 mm^3 detector biased at 1600 (left), 2200 (middle) and 3000 (right) V. The detector performance remains practically unchanged down to 1600 V.

2.5.3 Linear array of six 5x5x7 mm^3 VFG detectors

The linear array [21,22] consisted of VFG detectors fabricated from 5x7x25 mm^3 CZT crystals acquired from Redlen, Inc. The number of crystals was dictated by the size of the detector board, which we adopted from our previous project. The detectors have a simple design. Each crystal, furnished with two gold contacts on the top and bottom surfaces (the anode and the cathode), is encapsulated inside the ultra-thin polyester shell for electrical insulation and mechanical protection of the detector as we previously described. The shell tightly envelops the crystal and holds in place two CuBe flat-spring contacts on the cathode and the anode faces. Four 5-mm wide pads, cut from copper adhesive foil, are attached over the shell near the anode side. The detectors were placed vertically on the detector board and gently pressed from the top using the cathode board having the decoupling capacitors and resistors. The anode spring contacts touch the designated anode pads on the board, while the charge-sensing pads were soldered to the board contacts. The signals generated by the incident photons on the anodes, cathodes and four position-sensing pads were routed to the corresponding front ASIC inputs (charge-sensitive preamplifiers). The decoupling circuitries are required for reading the signals from cathodes, which were biased at 2500-3000 V. Fig. 14 shows the image of the fully assembled array consisting of six detectors mounted on the readout boards.

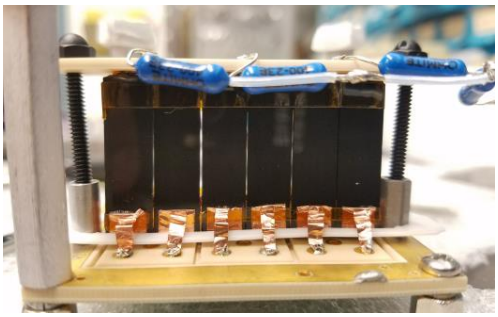

Fig. 14. Frontal view of the linear array with one side of pads connected to the PCB board.

The detector board, with the detectors on the front and the multipin connectors on the opposite side, was plugged into the motherboard inside the test box, see Fig. 15. The motherboard also carries the ultra-stable low-voltage passive converters supplying power to the ASIC chips, two analog-to-digital converters (ADCs) for digitizing the peak amplitudes from all channels, the Field Programmable Gate Array (FPGA) for processing the data and communicating with the ASICs, and the USB port.

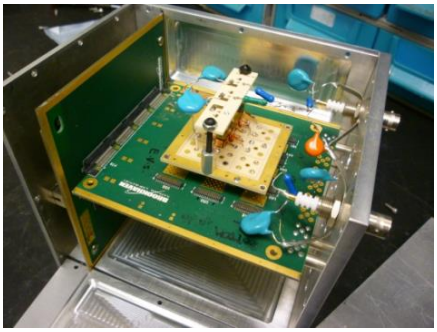

Fig. 15. Linear Array mounted to the circuit board inside the aluminum test box.

The AVG1 ASIC used in these measurements allowed us to capture the signals from individual cathodes, anodes and pads which would require 36 readout channels in the case of six detector arrays. The ASIC was developed for the conventional VFG detectors and employs the same design implemented for H3D pixelated detectors. The AVG ASIC has six inputs for the negative polarity signals induced on the cathodes and 36 channels with slightly shifted baselines so both polarity signals, which are generated in the pixelated detector, can be captured. One of our goals was to investigate the possibility of making a detector with a reduced number of readout channels. We tested several options of combining (using one input for reading signals from several pads or cathodes) the cathode and the charge-sensing pads. In the case of low-energy photons with low probability of having multiple interaction points, using the combined pads does not create any ambiguity problems related to the multiple interaction locations of the interaction points. We demonstrated that we could combine several pads belonging to the different detectors because there is no leakage current on the charge-sensing pads. Therefore, we were able to interconnect all pads in four groups and use only four individual inputs. We also demonstrated that two and even four cathodes could be connected to a single cathode input. Another goal was to evaluate the array in the field with real conditions. We fabricated a plastic enclosure, made of VeroBlackPlus RGD875, to hermetically seal the entire test box, see Fig. 16. A large aluminum back-side flange was used for heat dissipation of the enclosure. When the test box is placed inside the enclosure, the large flange touches a

copper block bolted to the back-side cover of the test box used for conducting the heat generated by the readout electronics and FPGA. Considering the high-temperature conditions expected for the field measurements, we attached a commercial 40W Peltier cooler to the outer flange to maintain a reasonably stable temperature, +/-1°C, of the detectors. As we show next, the main temperature instability does not come from the ASIC but from the charge collection efficiency of the detectors, which was found to be significant enough to affect the energy resolution if the temperature was not kept stable within 1-1.5 degrees. Using the environmental enclosure and the cooler, we were able to measure the detector responses measured at different temperatures between 15 and 40°C. As we found, the detectors could operate at a temperature close to 30°C without significantly affecting the energy resolution. Above 30°C the resolution degrades and approaches 2% at 662 keV at 40°C. We took only several measurements at temperatures above 35°C because, as we discovered, some of the detectors kept at high bias for several days in elevated temperatures suddenly became leaky and needed to be replaced. We limited the number of measurements taken at above 35°C to avoid damaging the detectors. We note that we fabricated and used a bulky environmental enclosure for the entire test box as it was the simplest (low cost) solution that could be implemented in preparation for the field tests. In the actual instrument, only the detectors and front-end electronics require environmental protection. As is seen in Fig. 16, the enclosure has specially designed slots for attaching the shielding tungsten plates and the front tungsten window, if necessary.

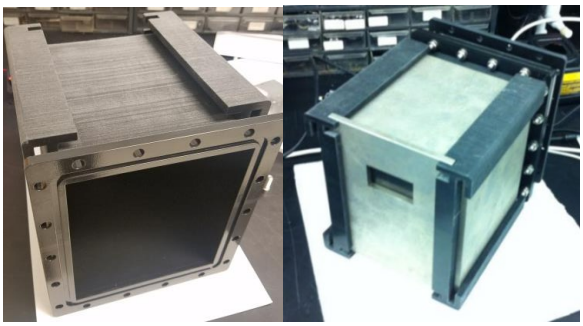

Fig. 16. (a) A 3D printed plastic waterproof enclosure. (b) Plastic waterproof enclosure with tungsten shielding plates.

The detectors' calibration was done for several temperatures and using several gamma-ray lines. For calibration we collected the pulse-height spectra from known gamma ray sources and used them to evaluate the channels' baselines, gains and the 3D correction matrixes for each detector. For presenting the results, we collected additional data sets (not used for calibration) to avoid any correlation effect, e.g., if we apply the correction matrix to the same data used for its evaluation, we can get the energy resolution as good as 0.3% at 662 keV, which is an erroneous result. Fig. 17 shows three rows of the spectra: after applying 3D corrections (top), 1D (middle) correction, and the raw data (bottom) measured from a fresh fuel rod, ~93% ^{235}U, located ~40 cm from the detectors plane. The measurements were taken at a temperature of ~19 °C. The same cathode bias of 2750 V was applied to all detectors. Fig. 18 shows the combined spectra after 3D and 1D correction. The energy resolution was found to be 1.9% FWHM at 186 keV, which is very good for such big detectors with an area of 5x7 mm^2. If we only apply a 1D correction, the energy resolution is only ~3%. We note that the electronic noise (due to leakage current) is the major factor limiting the energy resolution of these detectors.

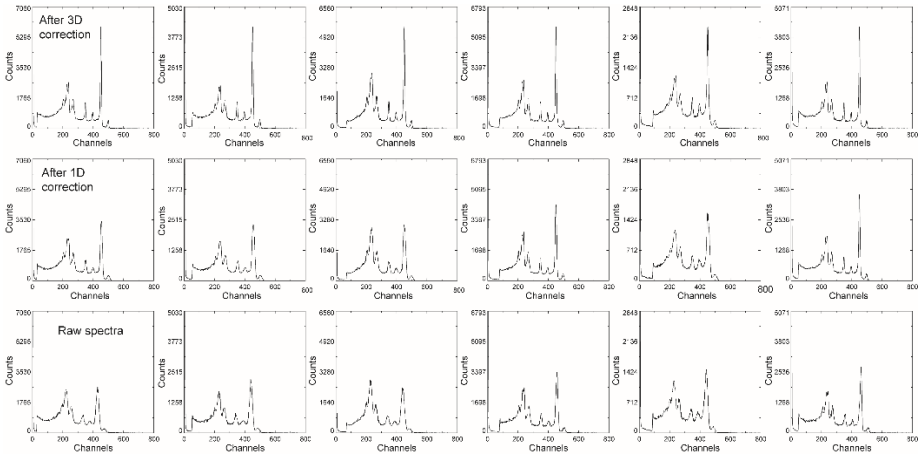

Fig. 17. The pulse-height spectra measured at 19°C and corrected using calibration data measured at the same temperature.

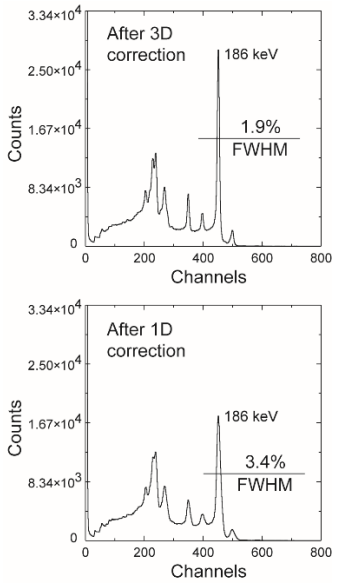

Fig. 18. The combined spectra, for ^{133}Ba, from all six detectors after (top) and before (bottom) 3D corrections.

Similarly, to the previous plot, Fig. 19 shows ^{133}Ba spectra measured at 20°C. The cathode bias is 2500 V. The bottom row shows the raw data clearly displaying a poor resolution for the multiple peaks close to each other. The middle row is the spectra after 1D correction. The top row shows a significant improvement in the resolution, visibly distinguishing the 303 keV peak from the 356 keV and 383 keV peaks.

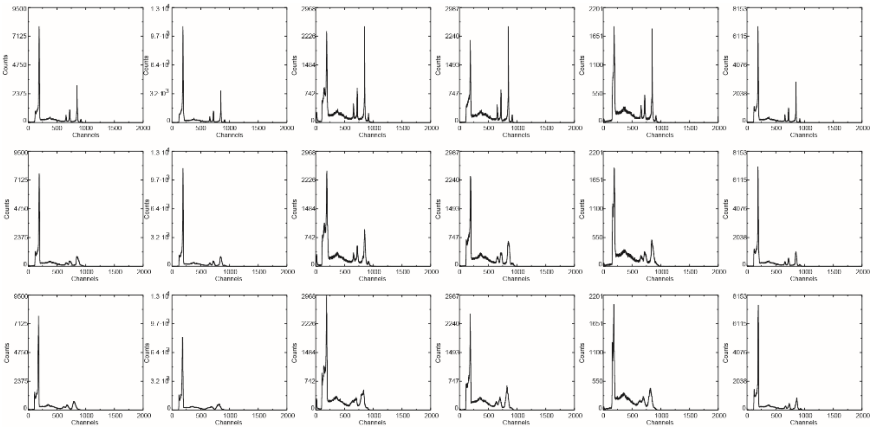

Fig. 19. ^{133}Ba spectra measured at 20C. The cathode bias is 2500 V.

Spectra in Figs. 20(a-f) illustrate the weak temperature dependence of the correction matrix. The ^{137}Cs spectra (a) and (b) were measured at 31°C and processed using the correction matrix generated for a 662 keV gamma line at 31 and 18°C, respectively. The spectra (c) and (d) were measured from two sources: ^{232}U and ^{137}Cs at 18°C and processed using the correction matrix generated for a 662 keV line at 31°C and 18°C. We note, that in these examples, the correction matrix generated at 662 keV works very well for low energies, e.g., 238 keV. Finally, spectra (e) and (f) from ^{232}U were measured at 31°C and processed using the correction matrix generated for a 662-keV gamma line at 31 and 18°C, respectively.

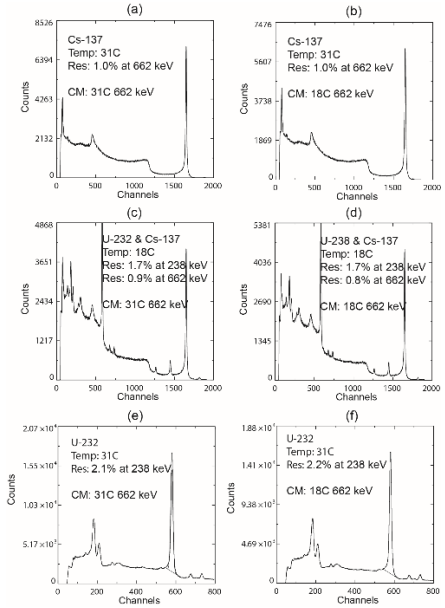

Figs. 20(a-f). Combined spectra from six detectors illustrating temperature independence of the correction matrix (CM). The Cs-137 spectra (a) and (b) were measured at 31C and processed using CM generated using a 662-keV line at 31 and 18°C, while the spectra (c) and (d) were measured from two sources: U-232 and Cs-137 at 18°C and processed using CM generated using 662-keV line at 31°C and 18°C, as well. Spectra (e) and (f) are from U-232 measured at 31°C and processed using CM generated using a 662-keV line at 31 and 18°C, respectively.

2.5.4 2x2 array of 6x6x20 mm3 VFG detectors fabricated for FLIR

We developed a robust detector module based on the 2x2 array of position-sensitive VFG CZT detectors and BNL-designed readout ASIC for assembling large-area high-energy resolution gamma-ray detection instruments. The array utilizes 6x6x20 mm^3 CZT crystals encapsulated inside ultra-thin polyester shells, and shielding strips placed near the anodes. We demonstrated an energy resolution of 1.0% at FWHM at 662 keV. We showed that the detectors can be grouped into sub-arrays with their cathodes connected to form a single electrode (a common cathode). The signals generated on the common cathodes are then used for electron charge-loss correction in the VFG detectors, and for rejecting incomplete charge-collection events. The position-sensitive side pads were used successfully to correct for material imperfections in CZT detector-grade crystals, which have plagued the technology for many years. We also demonstrated that the use of position-sensitive side pads improves greatly the acceptance rate for useful CZT crystals, and thus the novel design is expected to steadily lower the cost of detectors over the coming few years. Another important feature of the array is the ability to replace individual detectors to match their performances and correct for damage from handling. For replacement, the detector can be simply slid into the thin-walled honeycomb and electrically connected via the spring contacts. Fig. 21 shows a 2x2 array prototype assembled with 20-mm long crystals.

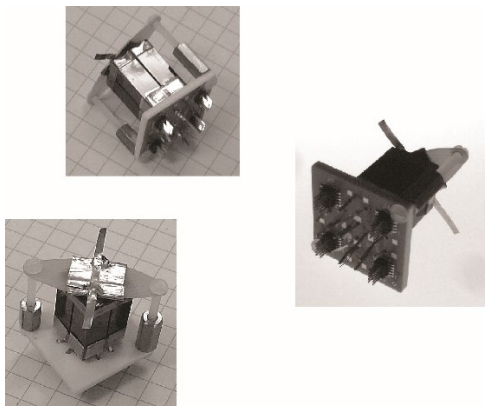

Fig. 21. A 2x2 array prototype of 7x7x20 mm^3 VFG detectors.

Several test measurements were carried out with these arrays to investigate their energy resolutions, stability of the correction matrix, and different charge-correction schemes. As an example, Fig. 22 shows the pulse-height spectra measured with a 2x2 array prototype of 7x7x20 mm^3 position-sensitive VFG detectors. In this example, we used four strips to evaluate the positions of the interaction points.

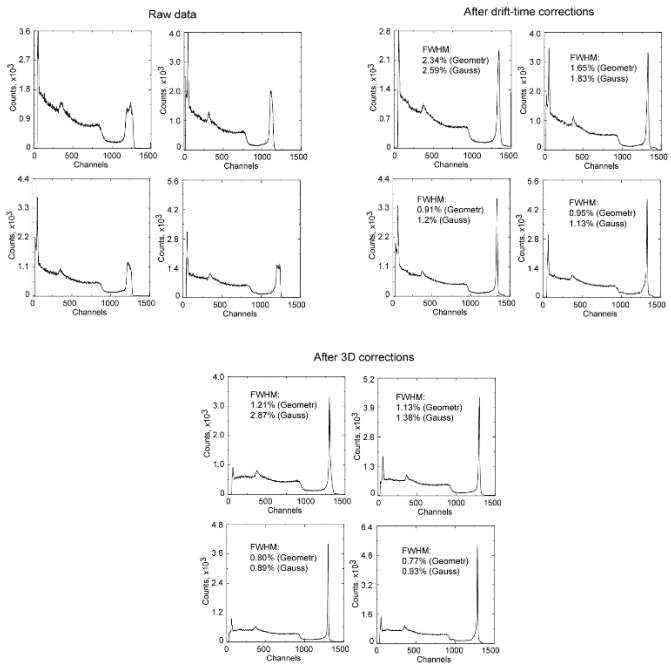

Fig. 22. Pulse-height spectra measured with the 2x2 array prototype of 7x7x20 mm^3 position-sensitive VFG detectors. The crystals used in the array were acquired from eV Products. In this array, we use the readout sharing approach: every two adjacent strips shared a single readout channel. Only single detector events were selected. Four position-sensing strips were used to evaluate the position of each event.

2.6 POSITION SENSING

The position-sensitive VFG detector operates as a mini time projection chamber (TPC) [23]. The amplitudes of the signals captured from the pads are used to evaluate X-Y coordinates while the measured drift time or the cathode-to-anode ratio, C/A, is used to independently evaluate the Z coordinates for the location of each interaction point. Fig. 23 shows the coordinate system associated with the VFG detector. For each pad we can obtain dependence of the pad amplitudes versus the *X-Y* coordinates of the electron cloud, which we call the pad response function, *A=R(X,Y).* Thus, the two-dimensional configurational space of the signal amplitudes measured from any pair of orthogonal pads has a one-to-one correspondence with the two-dimensional geometrical space *(X,Y)*. The response functions can be evaluated during the calibration or numerically calculated. Therefore, four estimates can be obtained for *X-Y* coordinates using the signals from two pairs of the orthogonal pads:

$$(X, Y) = R^{-1}(A_x, A_y). \quad (1)$$

Combing these estimates, we can write:

$$X = \sum_{i=1}^{4} X_i W_i \quad (2)$$

where W_i are the weights. A similar equation can be written for *Y* coordinates. Again, there could be several ways for finding the weights. For example, one can choose W_i proportional to the pad amplitudes *A*. We note, that the above equations can be applied in the cases of using only 2- and 3-pad signals to resolve the ambiguity problem mentioned before. Using a linear approximation for the response functions for all detectors and all pads, we can get a first order estimate for *X* and *Y* coordinates (the center of gravity method):

$$X = \frac{A_x^1}{A_x^1 + A_x^2} \quad (4)$$

and

$$Y = \frac{A_y^1}{A_y^1 + A_y^2} \quad (5)$$

The center of gravity method works well for correcting the response non-uniformity, but it causes notable image distortions near the detector edges, especially in the case of 2- and 3-pad signals. As we demonstrated [10], the experimentally evaluated response functions provide the excellent local XY position resolution of less than 100 μm at ~600 keV, which ensures the detector capability to correct the response non-uniformity. However, the geometrical position resolution (with respect to the detector boundaries), ~0.5 mm, is primarily limited by the local non-uniformity of the electric field which is common problem of CZT detectors.

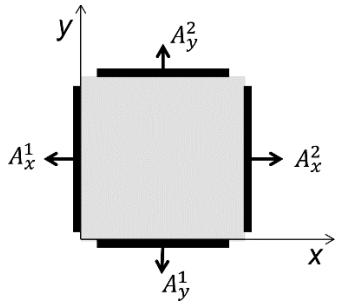

Fig. 23. Coordinate system associated with the position-sensitive VFG detector.

An alternative approach to the gravity formula is to use the actual response functions of the pads, which can be experimentally measured or calculated. The pad response functions, *A=R(x,y)*, are defined as a dependence of the pad amplitudes, *A*, on the *X-Y* coordinates giving a position of the electron cloud. The signal amplitudes measured from two pairs of the orthogonal pads form a 2D configurational space (signal amplitudes domain). Each point (A_x,A_y) from the amplitude domain corresponds to a point from the geometrical space *(X,Y)* domain, which means that four estimates can be obtained for *X-Y* coordinates using the signals from two orthogonal pads. In practice, during the calibration one should evaluate two transformation matrixes, representing the inverse response functions, and apply them to evaluate *X* and *Y* coordinates. We note that several matrixes can be generated for different Z segments to improve the accuracy. In this work, we used a single set of matrixes applied to all positions along the Z direction.

Figure 24 (left) illustrates the experimental setup used to evaluate the position resolution of a 10x10x32 mm^3 detector biased at 3700 V. A 0.8-mm wide slit in a 26-mm thick tungsten collimator was placed 65 mm above the detector's cathode. Here, we use a higher bias than we would normally use for spectroscopic measurements to suppress the local electric field variations and to achieve a better position resolution. A ^{137}Cs source was placed 27 cm above the collimator as shown in the figure. Fig. 24 (right) shows the image of the slits after combining all the single point photo absorption events distributed over the entire thickness of the 32-mm-thick detector. A pixel size in the map in Fig. 24 is 0.2 mm. The integrated event distribution with respect to the line representing the center of gravity of the image is shown at the bottom. The FWHM was found to be 14 pixels or 2.8 mm. By comparing this distribution with a Monte-Carlo simulated one for the same geometry, we estimated the spatial resolution to be ~1

mm. For the future, we are planning to use a collimated high-energy gamma-ray beam available to evaluate the position resolution with better accuracy and higher confidence.

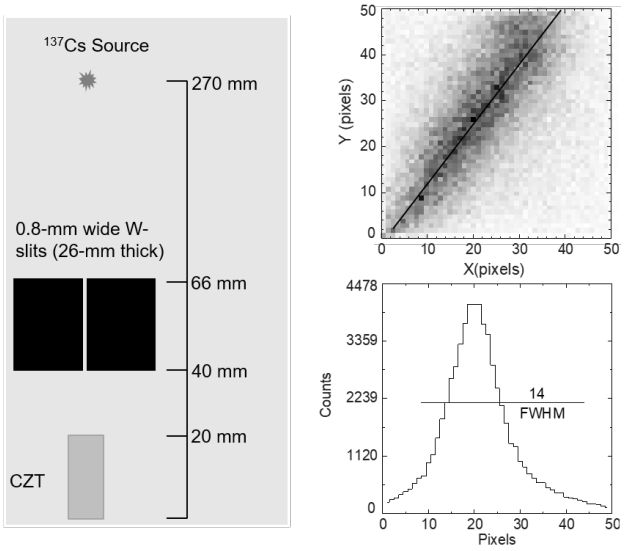

Fig. 24. A schematic of the experimental setup used to evaluate the position resolution of one of the 10x10x32 mm^3 detectors biased at 3700 V (left); an image of the slits after combining all the single point photo absorption events over the entire length of the 32-mm-thick detector (top-right); an event distribution with respect to a line representing the center of gravity of the image (bottom-left). FWHM is 14 pixels or 2.8 mm.

3. MEASUREMENTS OF URANIUM ENRICHMENT AT WESTINGHOUSE FUEL FABRICATION FACILITY

The successful benchtop demonstrations of the position-sensitive VFG detectors allowed us to carry out field measurements at LLNL, SRNL and the Westinghouse Fuel Fabrication Facility at Columbia, SC. The main goal of these measurements was to demonstrate the feasibility of enrichment measurements of the UF_6 storage cylinders. The first run of measurements took place in March of 2017. LANL, LLNL, SRNL, and BNL participated in these measurements with different assigned tasks, including currying out measurements with special sources, data analyzing and software development. Two detector configurations were tested: the linear array and the 4x4 array described above. SRNL transported equipment from SRNL to WFFF. Each UF_6 cylinder measurement has an acquisition time of 10-20 minutes. Some selected cylinders were measured 3 times at different locations along the axis to quantify reproducibility. Allowing time for moving the cylinders, it should be possible to acquire data from 8-12 cylinders in a day. BNL acquired and store the CZT array data, which were then be copied and distributed to the team at the end of the day, using USB drives. LANL acquired data during the same period using an HM-5 handheld detector with the IAEA-approved safeguards software package, and to share with the team the enrichments measured. Originally, we planned to investigate 15 cylinders with enrichments between 2.5% and 4.6% were measured, however measuring all 15 cylinders was not achieved due to time constraints. After calibration the detectors at LLNL, we were able to evaluate the enrichment of ~10 investigated cylinders. The high humidity and temperature affected performance of the

detectors, which were not hermetically sealed. We did not achieve the expected energy resolution and detectors response stability.

Several lessons have been learned during these tests. (1) The linear array was proved to be the most promising detector design for the enrichment measurements; (2) the detectors and readout electronics demonstrated good performance and stability during the measurements; however, (3) the temperature- and humidity-related effects need to be better understood and addressed accordingly. For these purposes, we carried out a series of measurements in the lab to verify the temporal and temperature stability of the detectors and ASIC. A small gain drift of the detectors with temperature can be mitigated by using device calibration. As we anticipated, it is very important that the detectors and the front ASIC have to be environmentally protected (encapsulated) to eliminate detrimental effects related to the accumulation of the moisture caused by the high humidity during the field measurements. In addition, we are optimizing the detector design and readout concept with the goal to simplify the instrument fabrication to reduce its cost and improve its reliability. All these problems were addressed and several improvements were implemented in our next detector , the most important of which was enclosing an entire test box (Fig. 25 and 26) inside a waterproof sealed 3D printed plastic housing (Fig. 27) and adding a small Peltier cooler to the backside flange (Fig. 28). The flange was attached to the internal text box via a copper cool finger. By cooling the outer flange were able efficiently to sink the heat generated by FPGA and ASIC and maintain a desired temperature of the detector board (the board on which 6 CZT detectors were mounted). The plastic enclosure was fabricated with special slots on the outside wall for inserting five tungsten plates which forms a collimator and shields the detectors from all other directions.

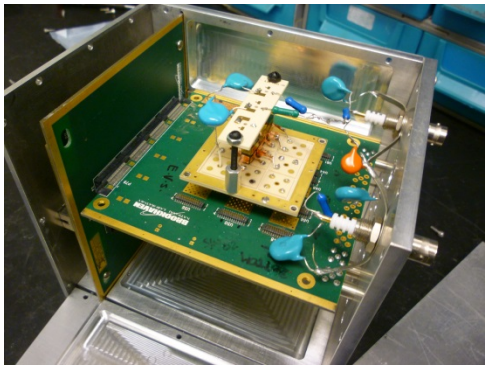

Fig. 25. Linear array mounted inside the test box

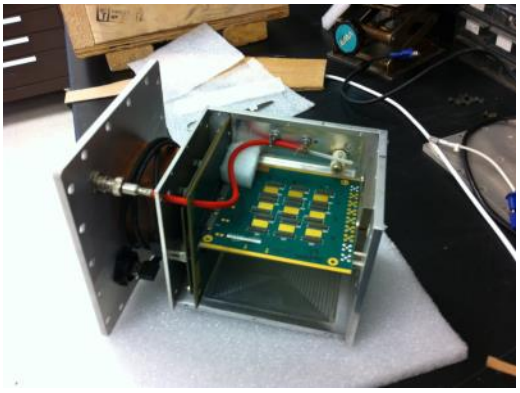

Fig. 26. Test box with the external flange

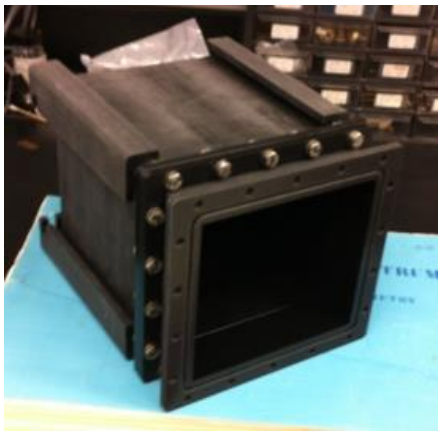

Fig. 27. 3D printed plastic waterproof enclosure

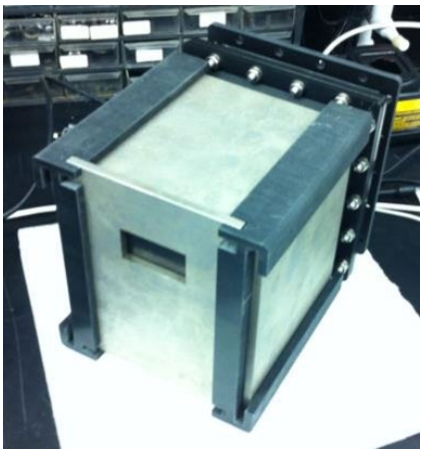

Fig. 28. Plastic waterproof enclosure with tungsten plates slid inside the slots

The second round of tests in SRNL and WFFF were carried out in September 17-21. We were much better prepared, had better detectors and the whole detecting system was enclosed inside the waterproof enclosure with the ¼ inch thick tungsten shielding and a well-designed collimator that fitted geometrically to the detector array. Prior to the measurements in field environments, we calibrated a thermocouple on the ASIC with respect to the temperature of the detector board. These calibrations were done in the lab by using the unsealed detector and an additional thermocouple attached to the detector board in a close proximity to the detectors (< 1 cm). In the current configuration, the temperature on the detector board is 0.7 degree higher than temperature readings from the ASIC thermocouple.

The detector calibrations were carried out using a fresh fuel element (97% U-235) available at BNL. We generated several calibration data sets at several temperatures and for different ASIC settings. At the end, during the actual measurements, we chose just one setting that ensures sufficiently good detector performance. Fig.29 shows the spectra evaluated using the best set of the calibration data. Fig. 30 shows the combined spectra after and before 3D corrections. The energy resolution is 1.9% FWHM at 186 at ~19.5C. This is a very good result for such detectors with length as great as 25 mm between anode and cathode. The electronic noise due to leakage current is the major factor that limits the energy resolution of the detectors.

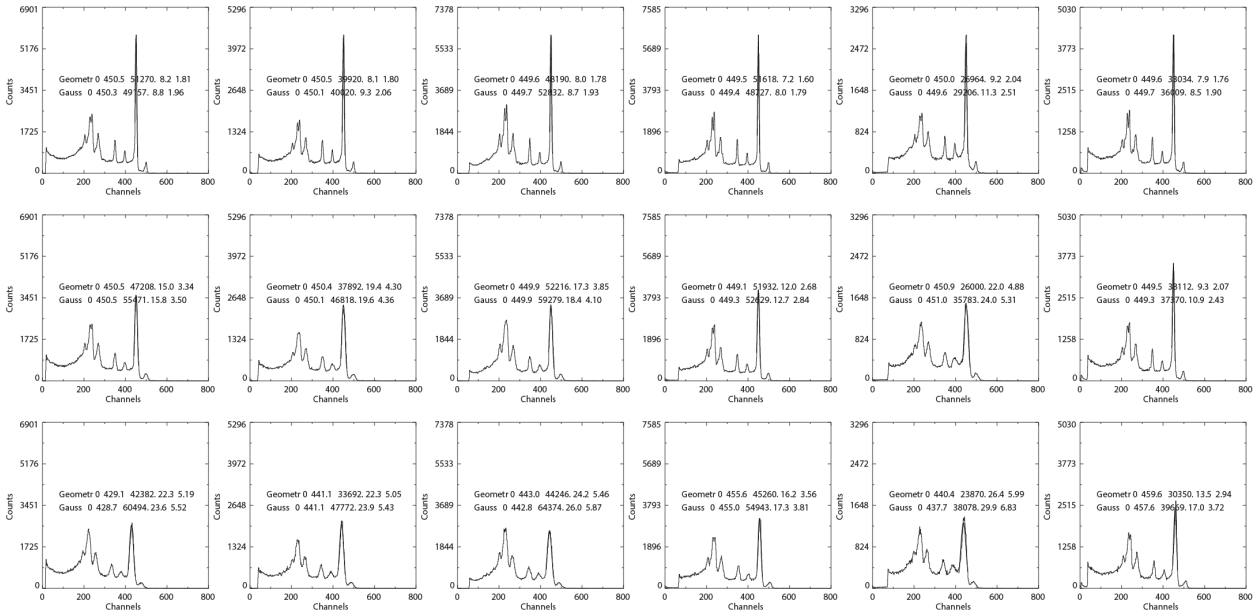

Fig. 29. The pulse-height spectra evaluated using the best set of the calibration data. Temperature is 19.5 C.

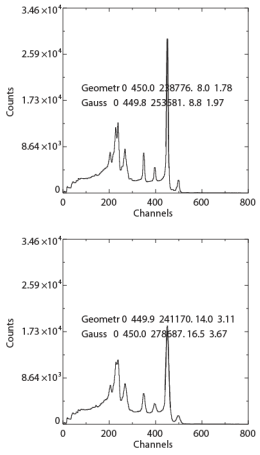

Fig. 30. The combined spectra from all 6 detectors after (top) and before (bottom) 3D corrections.

The calibration files included two sets of data: (1) baseline and gain calibrations for each of the detectors, and (2) 3D correction matrix. These two sets of data can be generated and used independently. The first sets of data can be generated “on the fly” during the measurements and requires a small amount of data collected for 1-2 min. Because of the temperature effect these files must be recalibrated before actual measurements to reflect any changes of temperature. We did this at SRNL. The second set of calibration data used for applying the 3D corrections are less sensitive to the temperature variation. During the field measurements we used the file generated at BNL at the temperature of 19C.

It is well-known that the ambient temperature changes affect charge collection efficiency in CZT detectors, which raises a question about temperature stability of the correction matrix. Can we use a correction matrix generated at a certain temperature apply the charge-loss corrections at other temperatures? A detector calibration procedure includes two steps. First, we calibrate the detector

baselines and gains using the standard sources, e.g., Cs-137 or U-232. The second step is to generate the correction matrix. By definition, the correction matrix is a ratio between a charge signal generated in a particular voxel and the average charge signal generated from all voxels, meaning that it should be independent on the detector gains and deposited energy. During the field measurements we kept the temperature of the detectors in the range 18-19 C. All detectors worked well without showing any degradation over time. We did not observe any effects related to the outside humidity and temperature. The outside temperature was in the range 25-35 C (early in the morning and in the midday) and humidity was nearly 90%.

The detectors were disassembled before transporting them and reassembled at SRNL. The whole detector was calibrated using the standard U-sources with a range of enrichments. We also used the same data to generate the new calibration files for detector baselines and gains. As an example, Fig. 31 shows the pulse-height spectra measured from a NIST-446 source at SRNL. As seen, the energy resolution is in the range 1.7-2.2 FWHM % at 186 keV. Fig. 32 shows the combined spectra from all six detectors after and before corrections.

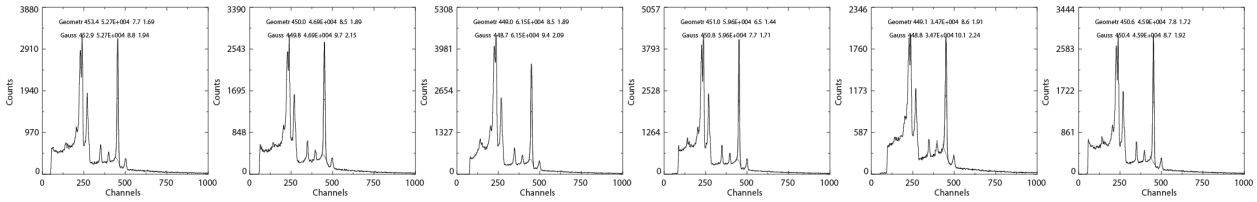

Fig. 31. The pulse-height spectra measured from a NIST-446 source at SRNL.

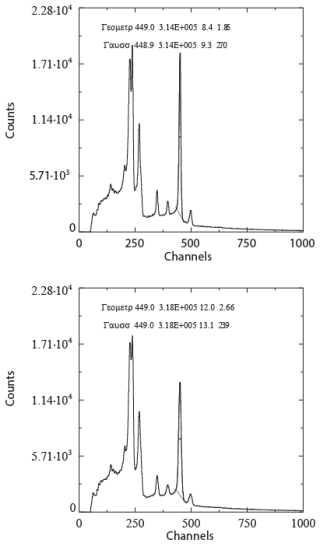

Fig. 32. Combined spectra from all six detectors, NIST-446 source.

Fig. 33 shows an example of the spectra measured from one of the UF6 cylinders. The first row contains the 3D corrected spectra (the rightmost plot is the combined spectrum). The second row contains the spectra after the drift-time corrections (1D correction). The third row shows the raw data.

Recalibrating the detector gains using the collected data we were able to slightly improve the spectra shown in the fourth row.

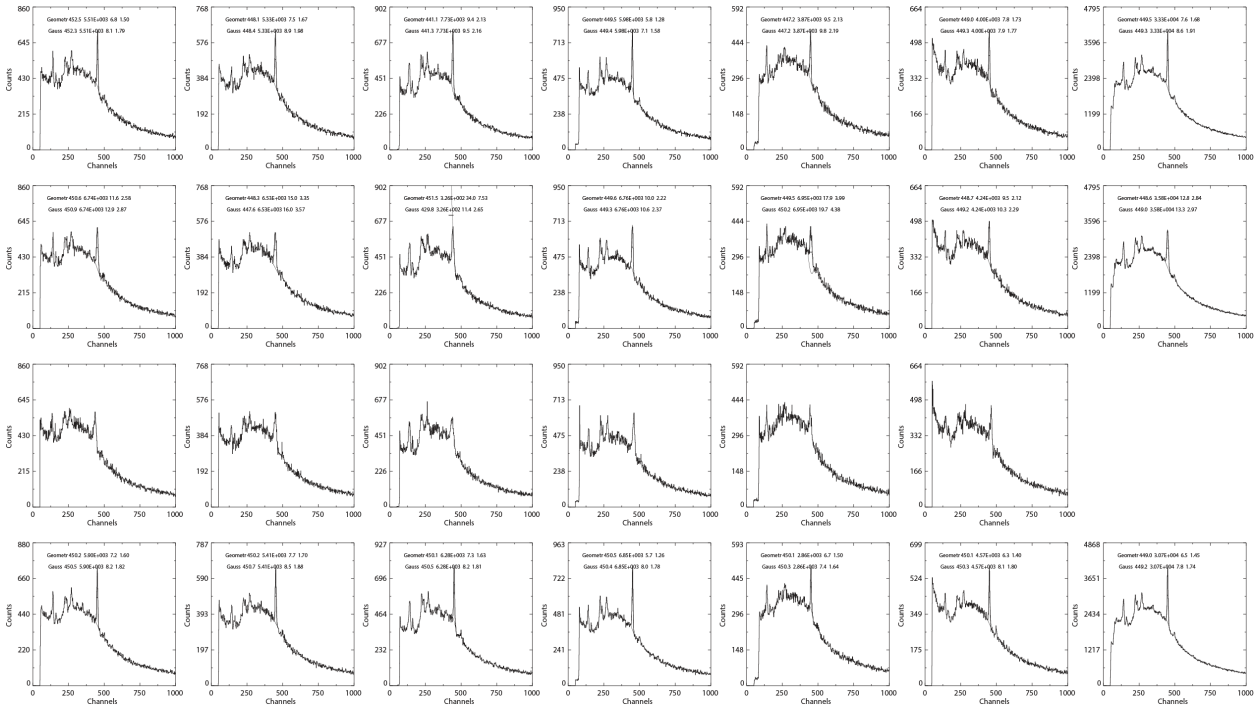

Fig. 33. Spectra measured from one of the UF6 cylinders. The first row contains the 3D corrected spectra (the rightmost plot is the combined spectrum). The second row contains the spectra after the drift-time corrections (1D correction). The third row shows the raw data. Recalibrating the detector gains using the collected data we were able to slightly improve the spectra (fourth row). The collection time is ~15 min.

The data for the cylinders measured at the Westinghouse Fuel Fabrication Facility (WFFF) can be analyzed to develop the CZT detector array into an enrichment meter device. The results of this analysis are shown in the figure below where we have plotted the count rate values for the 185.7-keV gamma ray as a function of the declared enrichment. The graph (Fig. 34) shows that the trend is quite linear with a strong deviation at the cylinder with a declared value of 4.4% enrichment. This low count rate behavior was also observed in the measurements performed earlier in the year. We will continue to analyze the data from the other detector systems to explain this anomaly.

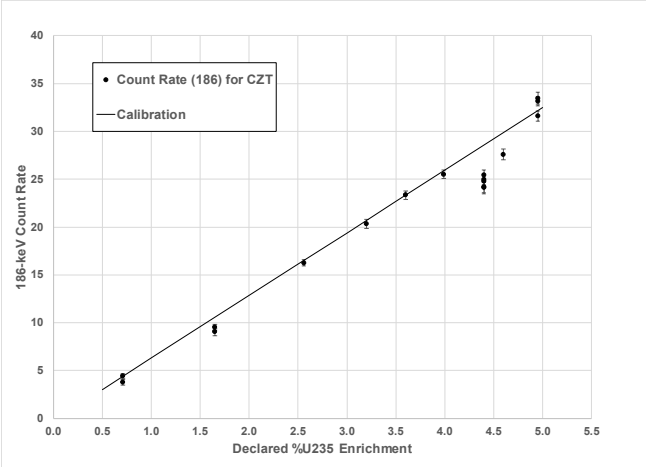

Fig. 34. Measured count rate values for the 185.7-keV gamma ray as a function of the declared enrichment.

Fig. 35. Pictures taken during the measurements at WFFF.

3.1 SOFTWARE DEVELOPMENT AND DATA ANALYSIS AT LLNL

LLNL has performed several analyses of the gamma-ray spectra that were acquired at the Westinghouse Fuel Fabrication Facility. An example of these data is shown in the Figure 36 below for several 30B cylinders with a range of enrichments. One can easily see the dependence of the intensity of 186-keV line on the enrichment of the cylinder. The data also demonstrates the high energy resolution of the gamma-ray spectrum which should help in enrichment determinations. For some of the measurements that occurred late in the day, the detector showed some anomalous behavior. We continue to analyze these data to determine if this behavior was due to environmental effects on the electronics or a mechanical issue with the alignment of the collimator.

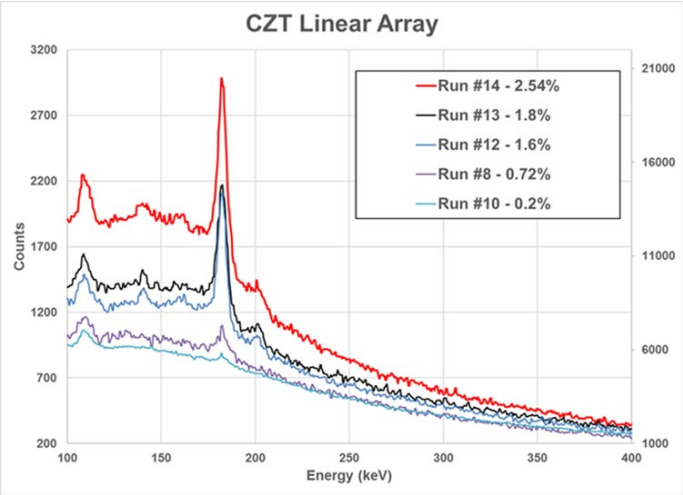

Fig. 36. Spectra of UF_6 with various enrichments measured using linear CZT VFG array

LLNL improved the Python-based CTZU code for the enrichment evaluation using data from CZT detectors. We began testing the code with data from uranium standards taken using a CZT5000S. The output from the analysis now uses standard Python libraries to display the calculated response from the ^{235}U, ^{238}U, and daughter products (see Figure 37). The CZTU analysis is strongly dependent on the peak fitting parameters, especially the low energy tailing component. We have begun characterizing this dependence and its effects to accurately determine uranium enrichment using CZT instruments.

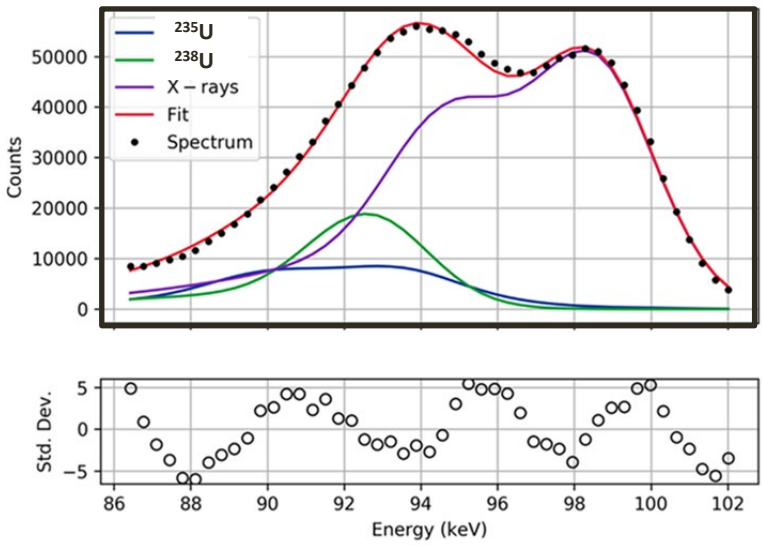

Fig. 37. Analysis of overlapping peaks

For a given enrichment, the test will measure the number of 186 keV gamma rays counted in a specified time, and the ratio of the peak area to the continuum counts in the same region of interest, obtained from count rates on either side of the peak. These parameters vary with the efficiency of the detectors and the amount of Compton scattering that occurs in a specific configuration (either in the U, the steel wall of the container, the collimator, the surrounding shield or the CZT itself). Statistical uncertainties can be derived from the numbers of counts. Other uncertainties can be estimated by repeated measurements in the presence of different attenuators and/or competing sources. The ultimate intended customer is the IAEA inspector who is required to check the enrichment of large numbers of uranium samples to verify the declarations of inspected parties. It also could be used by facility operators to quickly check the enrichment of cylinders entering their yard upon receipt.

An example of our results is the spectrum of the 30B cylinder with 4.95% enrichment (Fig. 38). The peak intensity of the 186-keV gamma ray can be determined by fitting the data to a Gaussian shape with a low-energy tail.

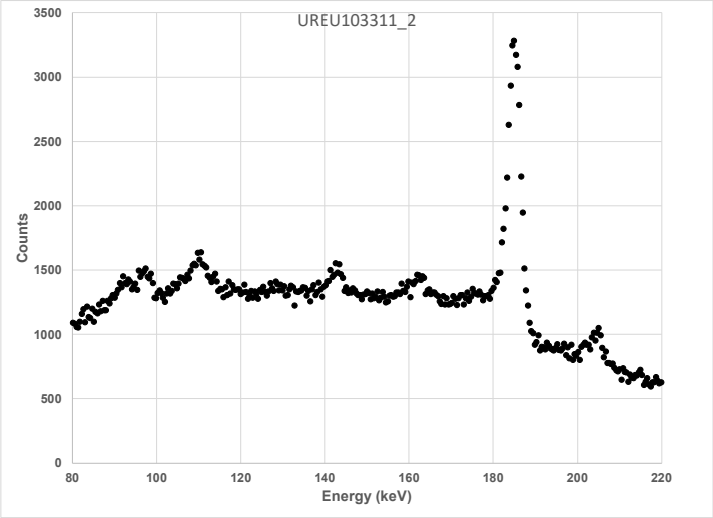

Fig. 38. CZT spectrum of a 30B cylinder with enrichment of 4.95%.

These data provide insight into how we can develop the CZT detector array into an enrichment meter device. The results of this analysis are shown in Fig. 34 above, where we have plotted the count rate values for the 185.7-keV gamma ray as a function of the declared enrichment. The graph shows that the trend is quite linear with a strong deviation at the cylinder with 4.4% enrichment. This low count rate behavior was also observed in the measurements performed earlier in the year.

The plot shows that there is a smooth linear relationship between the count rate and the declared enrichment except for the point a 4.4%. This point represents the cylinder with identification number UREU100447. This cylinder was also measured in the March 2017 measurement campaign and also showed a low count rate at that time. This cylinder seems to have a much higher count rate than the others. This is probably due to “hot spots” of daughter products that have built up in the cylinder. One can see this by examining the shape of the spectrum for this cylinder and comparing this to the spectrum for the 4.95% cylinder. This is shown in Fig. 40 below. One can see the large bump in the spectrum from the enhanced bremsstrahlung from the Pa-234m beta decay. We have also observed this in the HM-5 measurements. We used the HM-5 to measure at several locations on the cylinder. Fig. 41 shows two 100-second counts for the “usual” measurement spot versus that for the position of the CZT measurements. One sees that the count rate is more than double for the CZT position. We made similar comparisons with the HPGe detector and observed similar behavior.

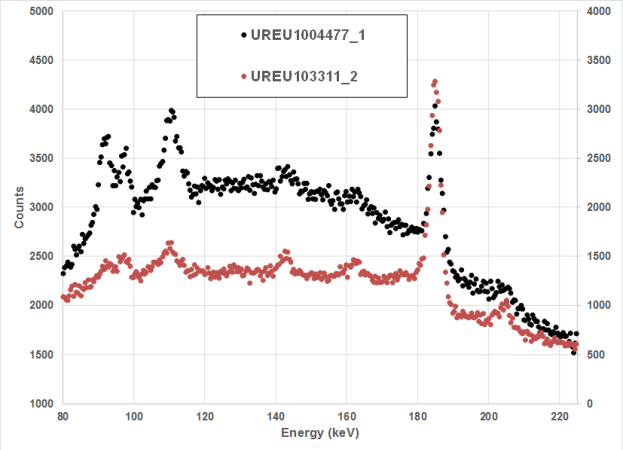

Fig. 40. Comparison of the spectra for cylinders with 4.95% and 4.4% enrichment.

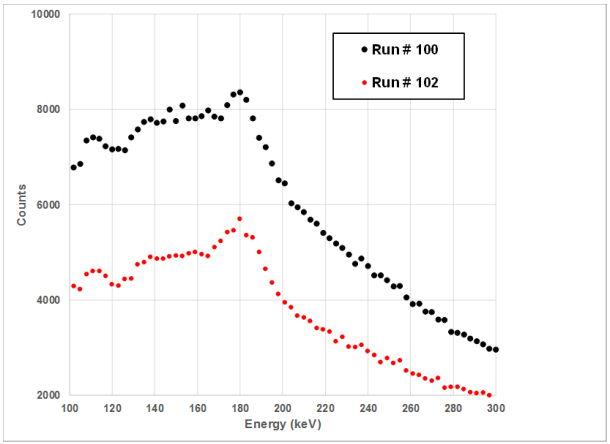

Fig. 41. Comparison of two spectra acquired by the sodium iodide-based HM-5 detection system for the same acquisition time. The upper data corresponds to the location where the CZT measurements occurred.

The low value of the derived 186-keV count rate for the CZT detector for this cylinder might be related to the higher count rate for these measurements. As a result, the team investigated the calculation of the dead time of the detector system and its behavior at high count rates. In addition, the BNL team conducted several test measurements in the lab to understand the effects of the count rate on the detector dead times. These measurements allowed us to understand the discrepancy in the data collected for the UREV1004477 cylinder. Using several strong Cs-137 sources we recreated the high-count rate conditions similar to that we had during the field tests. We observed that USB communication port we used to transfer the data was not fast enough. The problem was traced back to the original ASIC and DAQ firmware provided by the ASIC developers. A program error and some other deficiencies were identified in the original firmware. These problems, which resulted in the software missing some detected events from the data stream, never showed up in the lab environment. So, we were unable to correctly evaluate the detector's dead times at the count rates above 2 kHz, which was the case when we measured the UREV1004477 cylinder. Even though the ASIC can handle the rates up to 10 kHz, the DAQ firmware was unable to save all events on the hard drive. The ASIC designers corrected these problems and provided

updated firmware for the next field measurements. With the new firmware, we were able to measure the count rates almost up to the ASIC limit. We used two 3-4 μCi ^{137}Cs sources placed ~6 cm away from the array mounted inside the sealed box with the W shielding plates (same detector geometry used in the WFFF measurements). The dead times were calculated as a product of the ASIC reading time, 78 μs, and the total number of counts. The above measurements and data analysis conducted at BNL and LLNL helped us to identify an error in the ASIC firmware and understand and resolve the discrepancies measured for the UREV1004477. With the new firmware, we will be able to measure the count rates almost up to the ASIC limit.

4. FLIR EFFORTS

During the project, BNL regularly met with FLIR including by a face-to-face meetings and by routine teleconferences to obtain detailed design information of the nanoRaider. We also discussed the plans for the project with NA241 program managers and IAEA inspectors to get input from the end-user perspective. Fig. 31 (a) shows the current nanoRaider device and (b) illustrates its internal layout and plan for the new nanoRaider-AVG. The current nanoRaider device has three 15x13x5mm^3 CZT detectors (one for spectroscopy and two for counters) in the front. We planned to replace them with a 2x2 VFG array that has a total volume of 12x12x20 mm^3. The detection efficiency of the new detectors was expected to be comparable to the existing device, but the energy resolution will be much better. Because the new detector module would have been about 15 mm longer than the existing ones in the nanoRaider, we planned to extend the housing of nanoRaider by 15-20 mm.

From the discussions with FLIR, we learned that interfacing BNL's ASIC with the existing processor in the nanoRaider may be difficult, because the nanoRaider processor is an obsolete component and has very limited input/output ports to new detectors. Because of this, we considered two approaches for the nanoRaider-AVG: (1) design a stand-alone detector module with its own digital signal processor. The module will communicate with the nanoRaider-AVG via USB port; and (2) since FLIR was migrating its products to a new FPGA-based platform, we also considered the design of a detector module that can interface with this new platform. Both approaches are being discussed and evaluated with FLIR right now. Through careful analysis of FLIR's nanoRaider system, we discovered that many of the components can be used in the nanoRaider-AVG (e.g., power supply and software for identification), but some of the electronics are of a 10-year-old vintage and relatively obsolete today. As an example, the digital signal processor in the nanoRaider lacks the functionality to adequately handle the signal processing performed by BNL's DAQ. The easiest and quickest process is to modernize the electronics in the nanoRaider-AVG. We reached a final agreement regarding those components within the nanoRaider that are nearing the end of their logical lifecycle and may not be appropriate for use in the emerging nanoRaider-AVG. The staff capabilities to modernize the microelectronics in the nanoRaider-AVG existed within the BNL/FLIR team, and FLIR's commitment of resources to an upgraded instrument grew steadily as new data on the VFG detector module became available.

FLIR chose to use a set of hybrid preamplifiers as the front end and digitize the charge signals using their low-power compact in-house-developed readout system. Fabrication of the charge-sensitive hybrid preamplifiers by FLIR was a critical task for the instrument integration. The charge sensitive preamplifier will be used in connection with CZT detectors for gamma ray spectroscopy. Low noise, low power consumption, reasonable linearity, and high dynamic range over a wide temperature range are important design goals. The FLIR Oak Ridge team made good progress with the hardware design for processing

signals of a CZT detector with six electrodes. Prototypes of a discrete preamplifier and an ADC board were assembled. The ADC board was connected to an off-the-shelf FPGA development system. Raw detector signals were acquired with this setup. In addition, detector signals were captured with NIM electronics for verifying preamp functionality. The crystal with dimensions of 5x5x15 mm^3 used in these measurements was cut from an R300 15x13x5mm CZT detector.

Fig. 31 (a-d) documents the FLIR experimental setup with the light tight and shielded box, the wiring of the preamplifier with CZT crystal and the board with the analog-to-digital converters (ADC) and the field-programmable gate array (FPGA) connected at the outside via the twisted pair cables.

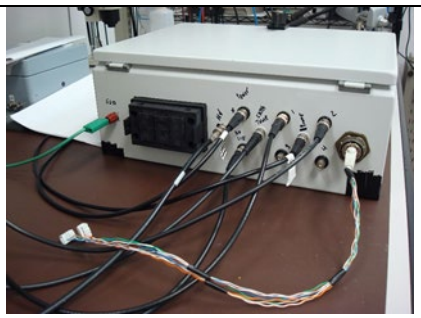

Fig. 31 (a). Light tight and shielded box for detector assembly.

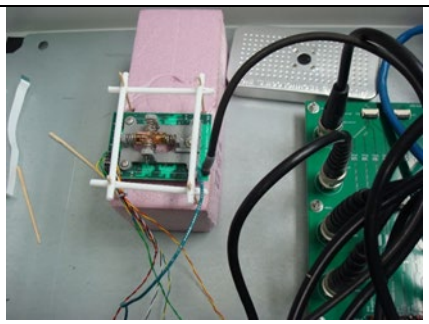

Fig. 31 (b). Preamp board inside box.

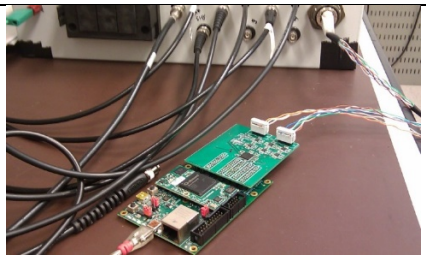

Fig. 31 (c). Preamp board inside box.

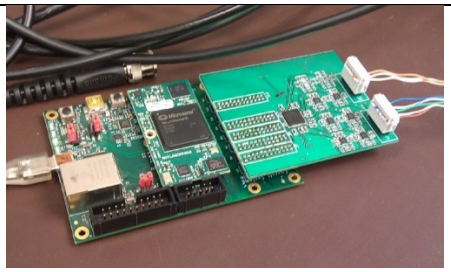

Fig. 31 (d). View of ADC board.

Originally, we planned to have a prototype version completed by FLIR and ready to test by the end of FY2017. FLIR completed the prototype designs and preliminary testing of the components, including readout electronics and CZT detector arrays. Unfortunately, due to FLIR's internal schedules, the tests were postponed and moved to the end of FY2019 and then moved further beyond the duration of the project. Even though the FLIR prototype was not for testing at WFFF within the time boundaries of this project, the BNL prototypes demonstrated the high performance of the VFG detector arrays for

enrichment measurements of UF6 cylinders in the field environments and their potential for use in practical handheld instruments.

Summary

The main objective of the project was to design and build an engineering prototype of an advanced gamma-ray spectrometer (nanoRAIDER-AVG) by incorporating Cadmium-Zinc-Telluride (CZT) virtual Frisch-grid detectors (VFG) (with 1% or better energy resolution) into the nanoRAIDER device, manufactured by the FLIR Corporation.

This project was a continuation of a project funded by the NNSA Office of International Nuclear Safeguards, which began in FY15. An improved nanoRAIDER with a high-resolution gamma-ray detector (CZT based) would help to answer IAEA inspection needs as described in the IAEA Long-Term R&D Plan, 2012-2023. Specifically, this continuing project would address the IAEA's need in LTRD 5.4 - recovering from loss on spent LWR fuel casks for partial defect (i.e., detect one missing rod from an assembly) with high confidence, which is also aligned well with the priority of NGSI Safeguards Technology Development Subprogram. In addition, the project addresses IAEA's needs under items 2.2 (elemental and isotopic signatures of fuel cycle processes), 2.3 (detect signatures of undeclared activity and improve analysis), 2.6 (detect process emanations), and 3.2 (fissile content of metal mixtures containing actinides Np, Am, etc.)

Four national laboratories participated in the project: BNL, LLNL, SRNL, and LANL. BNL worked on the instrument design, benchtop testing of the components, selecting electronics, and testing detector arrays using BNL waveform digitizing system. BNL and FLIR completed the detector array and design and optimization, the instrument's mechanical design, readout electronics and the signal processing algorithm. LLNL and LANL worked on the software development and enrichment calculation software tasks. The hardware and software components were delivered to FLIR according to the schedule. The data from the detector testing were analyzed and provided to NA-241. SRNL provided assistance in the detector calibration and taking measurements at the Westinghouse Fuel Fabrication Facility to measure enrichment in UF6 cylinders.

The FLIR Corporation, which manufacturers the HM-5 and nanoRAIDER, participated by providing in-kind support including design information for the original nanoRAIDER device and assisting BNL scientists and engineers in designing the nanoRAIDER-AVG. An NDA as put in place between BNL and FLIR to facilitate the sharing of such information. BNL has two patents issued regarding VFG detector technology: US-8586936-B2, Hybrid Anode for Semiconductor Radiation Detectors, and US-20130126746-A1, Array of virtual Frisch-grid detectors with common cathode and reduced length of shielding electrodes. In addition, BNL filed a third patent on position-sensitive VFG detectors to further advance commercialization of this promising detector design and low-power ASIC readout. BNL built and tested several detector prototypes, including a 2x2 array of 3D-VFG detectors coupled with the existing 36-channel ASIC specifically developed for 3D-VFG detectors for signal readout from these detectors. Two custom circuit boards were designed to interface these two parts to each other. The bench-top system, based on the 4x4 and linear arrays of 6x6x20 mm^3 position-sensitive VFG CZT detectors, was developed and tested during the field measurements at the Westinghouse Fuel Fabrication Facility. FLIR designed the first instrument prototype and readout electronics. Two field measurements were conducted at Westinghouse Fuel Fabrication Facility.

This project facilitated the collaborative efforts between BNL and FLIR to integrate the instrument prototype and demonstrate its performance to the sponsor. We developed and tested two prototypes of handheld instruments based on CZT detectors (with 1% or better resolution) for isotope identification and related safeguards applications.

As a recommendation for future work, it will be mutually beneficial to continue this development and provide support for FLIR. One of the important tasks will be to complete the prototype U enrichment detector design and carry out the field test at the Westinghouse Fuel Fabrication Facility to measure of enrichment in UF6 cylinders. The measurement of enrichment of stored uranium is a critical function for safeguards and nuclear materials accountability.

References

[1] C. L. Lingren, J. F. Butler, B. Apotovsky, R. L. Conwell, F. P. Doty, S. J. Friesenhahn, "Semiconductor radiation detector with enhanced charge collection", U.S. Pat. 5,677,539, 1997.

[2] K. Parnham, C. Szeles, K. G. Lynn, and R. Tjossem, "Performance Improvement of CdZnTe Detectors Using Modified Two-Terminal Electrode Geometry," in Hard X-ray, Gamma-Ray and Neutron Detector Physics, Proceedings of SPIE Vol. 3786, pp. 49-54, 1999.

[3] C. Szeles, D. Bale, J. Grosholz, Jr., G. L. Smith, M. Blostein, and J. Eger, "Fabrication of High Performance CdZnTe Quasi-Hemispherical Gamma-ray CAPture™ Plus Detectors", Hard X-Ray and Gamma-Ray Detector Physics VIII, edited by Larry A. Franks, Arnold Burger, and Ralph B. James, Proceedings of SPIE Vol. 6319 (SPIE, Bellingham, WA, 2006).

[4] "Improving the Performance of Quasi-Hemispherical CdZnTe Detectors Using Infrared Stimulation", P. Dorogov, V. Ivanov, A. Loutchanski, L. Grigorjeva, and D. Miller, IEEE Trans. Nucl. Sci. 59, n. 5, pp. 2375-2382, 2012.

[5] D. S. McGregor and R. A. Rojeski, "High-resolution ionization detector and array of such detectors", US Pat. 6175120, 2001.

[6] G. Montemont, M. Arques, L. Verger, and J. Rustique, "A Capacitive Frisch Grid Structure for CdZnTe Detectors", IEEE Trans. Nucl. Sci. 48, pp. 278-281, 2001.

[7] J. D. Eskin, H.H. Barrett, and H.B. Barber, "Signals induced in semiconductor gamma-ray imaging detectors", J. Appl. Phys., vol. 85, pp. 647-659, 1999.

[8] Z. He, W. Li, G. F. Knoll, D. K. Wehe, J. Berry, and C. M. Stahle, "3-D position sensitive CdZnTe gamma-ray spectrometers," Nucl. Instr. and Meth. A 422, pp. 173-178, 1999.

[9] A. E. Bolotnikov, K. Ackley, G. S. Camarda, C. Cherches, Y. Cui, G. De Geronimo, J. Fried, D. Hodges, A. Hossain, W. Lee, G. Mahler, M. Maritato, M. Petryk, U. Roy, C. Salwen, E. Vernon, G. Yang, and R. B. James, "An array of virtual Frisch-grid CdZnTe detectors and a front-end application-specific integrated circuit for large-area position-sensitive gamma-ray cameras," Review of Scientific Instruments, vol. 86, no. 7, 2015.

[10] A. E. Bolotnikov. J. Butcher, G. S. Camarda, Y. Cui, G. De Geronimo, J. Fried, P. M. Fochuk, A. Hossain, K. H. Kim, O. V. Kopach, G. Mahler, M. Marshall, B. McCall; M. Petryk, E. Vernon, Ge. Yang, R, B. James,

"Design Considerations and Testing of Virtual Frisch-Grid CdZnTe Detector Arrays Using the H3D ASIC", IEEE Trans. Nucl. Sci. 60, n. 4, pp. 2875-2882, 2013.

[11] L. A. Ocampo Giraldo, A. E. Bolotnikov, G. S. Camarda, S. Cheng, G. De Geronimo, A. McGilloway, J. Fried, D. Hodges, A. Hossain, K. Ünlü, M. Petryk, E. Vernon, V. Vidal, G. Yang, R. B. James, "Arrays of Position-Sensitive Virtual Frisch-Grid CdZnTe Detectors: Results From a 4x4 Array Prototype", IEEE Trans. Nucl. Sci. 64, n. 10, pp. 2698-2705, 2017.

[12] A. E. Bolotnikov, G. S. Camarda, E. Chen, S. Cheng, Y. Cui, R Gul, R. Gallagher, V. Dedic, G. De Geronimo, L. Ocampo Giraldo, J. Fried, A. Hossain, J. M. MacKenzie, P. Sellin, S. Taherion, E. Vernon, G. Yang, U. El-hanany and R. B. James, "CdZnTe Position-Sensitive Drift Detectors with Thicknesses Up to 5 cm", Appl. Phys. Lett. 108, p. 093504 (2016).

[13] Wonho Lee; Aleksey Bolotnikov; Taewoong Lee; Giuseppe Camarda; Yonggang Cui; Rubi Gul; Anwar Hossain; Roy Utpal; Ge Yang; Ralph James,"Mini Compton Camera Based on an Array of Virtual Frisch-Grid CdZnTe Detectors", IEEE Trans. Nucl. Sci. 63, n. 4, pp. 259-265, 2016.

[14] https://www.samtec.com/.../high-density-arrays/zray

[15] G. De Geronimo, E. Vernon, K. Ackley, A. Dragone, J. Fried, P. O'Connor, Z. He, C. Herman and F. Zhang, "Readout ASIC for 3D Position-Sensitive Detectors", IEEE Trans. Nucl. Sci., Vol. 55, no. 3, pp. 1593-1603, 2008.

[16] E. Vernon, K. Ackley, G. De Geronimo, J. Fried, P. O'Connor, Z. He, C. Herman, and F. Zhang, "ASIC for high rate 3-D position sensitive detectors," IEEE Trans. Nucl. Sci., vol. 57, n. 3, pp. 1536-1542, 2010.

[17] F. Zhang, C. Herman, Z. He, G. De Geronimo, E. Vernon, and J. Fried, "Characterization of the H3D ASIC readout system and 6.0 cm3 3-D position sensitive CdZnTe Detectors," IEEE Trans. Nucl. Sci., Vol. 59, pp. 236-242, 2012.

[18] Submitted to Nucl. Instr. and Meth., 2020.

[19] L. Ocampo Giraldo, A. E. Bolotnikov, G. S. Camarda, G. De Geronimo, J. Fried, D. Hodges, A. Hossain, K. Ünlü, E. Vernon, and R. B. James, "Using A Linear Array of Position-Sensitive Virtual Frisch-Grid CdZnTe Detectors for Uranium Enrichment Measurements", NIMA 903, pp. 204-214, 2018.

[20] A. E. Bolotnikov, G. S. Camarda, G. De Geronimo, J. Fried, D. Hodges, A. Hossain, K.Kim, G. Mahler, L. Ocampo Giraldo, E. Vernon, G. Yang, R. B. James, "A 4x4 array module of position-sensitive virtual Frisch-grid CdZnTe detectors for gamma-ray imaging spectrometers", In press, corrected proof, Available online 30 July 2018.

[21] Bolotnikov, G. S. Camarda, G. De Geronimo, J. Fried, D. Hodges, A. Hossain, L. Ocampo, G. Yang, K. Ünlü, E. Vernon and R. B. James, "Development of position-sensitive virtual Frisch-grid CdZnTe detectors", invited talk presented at SORMA XVII - June 11th, 2018 to June 14th, 2018 at the University of Michigan, Ann Arbor, MI.

[22] L. Ocampo Giraldo, A. E. Bolotnikov, G. S. Camarda, G. De Geronimo, J. Fried, D. Hodges, A. Hossain, K. Ünlü, E. Vernon, and R. B. James, "Using A Linear Array of Position-Sensitive Virtual Frisch-Grid CdZnTe Detectors for Uranium Enrichment Measurements", presented at INMM 59th Annual Meeting July 22 2018.

[23] D. R. Nygren, "A time projection chamber", presented at 1975 PEP Summer Study, PEP 198, 1975 and included in Proceedings.